

Review

# Breaking the Polarization Bottleneck: Innovative Pathways to High-Performance Metal–Air Batteries

Biao Ma <sup>1</sup>, Deling Hong <sup>1</sup>, Xiangfeng Wei <sup>1</sup> and Jiehua Liu <sup>1,2,\*</sup> 

<sup>1</sup> Future Energy Laboratory, School of Materials Science and Engineering, Hefei University of Technology, Hefei 230009, China

<sup>2</sup> Key Laboratory of Advanced Functional Materials and Devices of Anhui Province, Engineering Research Center of High-Performance Copper Alloy Materials and Processing, Ministry of Education, Hefei 230009, China

\* Correspondence: liujh@hfut.edu.cn

## Abstract

Metal–air batteries have excellent theoretical energy density and economic advantages through abundant anode materials and open cathode structures. However, the actual energy efficiency of metal–air batteries is much lower than the theoretical value due to the effect of polarization voltage during battery operation, limiting the power output and thus hindering their practical application. This review systematically dissects the origins of polarization: slow oxygen reduction/evolution reaction (ORR/OER) kinetics, interfacial resistance, and mass transfer bottlenecks. We highlight cutting-edge strategies to mitigate polarization, including atomic-level engineering of air cathodes (e.g., single-atom catalysts, low Pt catalysts), biomass-derived 3D porous electrodes, and electrolyte innovations (additives to inhibit corrosion, solid-state electrolytes to improve stability). In addition, breakthroughs in metal–H<sub>2</sub>O<sub>2</sub> battery design using concentrated liquid oxygen sources are discussed. Together, these advances alleviate the battery polarization bottleneck and pave the way for practical applications of metal–air batteries in electric vehicles, drones, and deep-sea devices.

**Keywords:** metal–air battery; polarization voltage; air cathode; electrolyte



Academic Editor: Elie Paillard

Received: 14 July 2025

Revised: 6 August 2025

Accepted: 15 August 2025

Published: 19 August 2025

**Citation:** Ma, B.; Hong, D.; Wei, X.; Liu, J. Breaking the Polarization

Bottleneck: Innovative Pathways to High-Performance Metal–Air Batteries. *Batteries* **2025**, *11*, 315. <https://doi.org/10.3390/batteries11080315>

**Copyright:** © 2025 by the authors. Licensee MDPI, Basel, Switzerland. This article is an open access article distributed under the terms and conditions of the Creative Commons Attribution (CC BY) license (<https://creativecommons.org/licenses/by/4.0/>).

## 1. Introduction

Driven by the continuous rise in global energy consumption and carbon neutrality targets, the development of new electrochemical energy storage technologies has become a strategic key to solving the energy–environment dilemma. As the most mature energy storage carrier in commercialization, Li-ion batteries rely on the intercalation reaction mechanism between layered oxide cathode (e.g., NMC811) and graphite anode to successfully achieve a mass energy density of 150–250 Wh kg<sup>−1</sup> [1,2], and their liquid system based on the LiPF<sub>6</sub> electrolyte derives a cycle life of more than 5000 cycles [3], which has directly contributed to the high-speed development of electric vehicles globally. However, due to the theoretical capacity limit of graphite anode [1] (372 mA h g<sup>−1</sup>) and the resource constraints of strategic metals such as cobalt and nickel [4], the existing system faces a fundamental challenge to achieve the 400 Wh kg<sup>−1</sup> target set by the Energy Saving and New Energy Vehicle Technology Roadmap 2.0.

As a third-generation high-energy chemical power source, metal–air batteries have attracted much attention for their breakthrough energy storage mechanism [5,6]. The remarkable theoretical energy densities of this system are metal-dependent: lithium–air (Li–air) batteries can reach theoretical values of up to 5900 Wh kg<sup>−1</sup>, zinc–air (Zn–air) batteries of up to 1220 Wh kg<sup>−1</sup> (Figure 1a), and aluminium–air (Al–air) batteries of up to 8100 Wh kg<sup>−1</sup> [7]. This allows metal–air batteries to show a unique advantage in extreme application scenarios, such as UAV endurance

and deep space probes. In terms of system economics, the advantages are high abundance of anode materials (e.g., Al accounts for about 8.23% of the earth's crust, which is much higher than the 20 ppm of Li resources, Figure 1b), which significantly reduces the cost, and the open cathode structure eliminates the need for expensive cathode materials (e.g., Li cobaltate) for conventional Li-ion batteries [8]. As the most technologically mature and commercially viable metal–air battery, Zn–air batteries have been commercialized in hearing aids and navigation lights due to their reversible deposition and closed-cycle design (ZnO electrolytic regeneration) [9]. Moreover, due to their high safety and stable voltage platform, Zn–air batteries have broad application prospects in the field of high-energy density micro-batteries and grid energy storage [10,11]. Zhang et al. used PVA–KOH– $K_2CO_3$  hydrogel electrolyte to reduce the electrolyte volume, achieving a volumetric energy density of approximately  $1400\text{ Wh L}^{-1}$  and an areal peak power density of  $139\text{ mW cm}^{-2}$  for micro Zn–air batteries. Through further structural optimization, including the use of multi-layer gel electrolytes and thinning of the air cathode, the volumetric and gravimetric energy densities reached  $1576\text{ Wh L}^{-1}$  and  $420\text{ Wh kg}^{-1}$ , respectively [12]. Therefore, Zn–air batteries are expected to become the most promising alternative to micro Li-ion batteries. As a primary battery, Al–air batteries exhibit an exceptionally prominent actual energy density. Additionally, Al is abundant in resources and low in cost. Currently, mature primary Al–air battery systems have been applied in special scenarios that require ultra-high energy density, long storage life (in dry state), and have no requirement for charging, such as underwater equipment and emergency backup power supplies [13,14]. The core appeal of Li–air batteries lies in their unparalleled theoretical energy density, making them a highly promising energy candidate for future electric vehicles and long-endurance drones. However, due to issues with cycle life and safety, Li–air batteries are still in the early stages of development. Currently, solid-state electrolyte modulation technology has helped Li–air batteries achieve a small polarization gap and high-rate operation [15]. In summary, we selected these three highly representative metal–air batteries as the research objects for polarization voltage. In Figure 1c, we searched the number of papers published on metal–air batteries from January 2015 to May 2025. The publication of metal–air batteries, especially Zn–air batteries, has steadily increased in the last decade, and these advances are collectively driving the critical turnaround of metal–air batteries from the laboratory to industrialization.

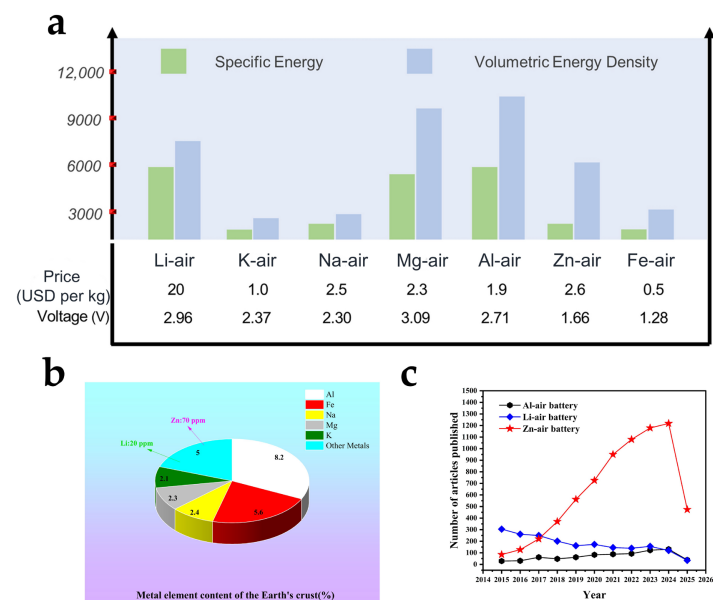


**Figure 1.** (a) Theoretical specific energies, volumetric energy densities, nominal cell voltages, and properties for various metal anodes (Adapted with permission from Ref. [16], Springer Nature 2024.); (b) Metal element content of the Earth's crust; data from the Israel Science and Technology Directory; (c) Number of publications per year from January 2015 to May 2025.

The loss of real energy efficiency due to polarization voltage has formed a significant techno-economic barrier [8,17]. The polarization voltage is the difference between the actual operating voltage and the theoretical equilibrium voltage of metal–air batteries, which is essentially caused by the combination of activation polarization, concentration polarization, and ohmic polarization. Polarization voltage causes the actual output voltage of the battery to be lower than the theoretical value, which results in lower efficiency [18], e.g., the actual energy density of Zn–air batteries is less than 60% of the theoretical value [19]. Moreover, the side reactions induced by the polarization voltage (e.g., hydrogen evolution reaction [20], dendritic crystal growth [21,22]) limit the power output, which affects the acceleration performance of the battery in high-power scenarios, such as the acceleration performance of an electric vehicle. In Figure 2, to further delve into the polarization voltage, this review summarizes the core causes of the polarization voltage in metal–air batteries: activation polarization due to the kinetic hysteresis of the oxygen reduction reaction (ORR) and oxygen evolution reaction (OER), concentration polarization due to oxygen diffusion and ionic diffusion, and ohmic polarization influenced by the interfacial resistance and electrolyte conduction. The corresponding solution strategies are also discussed in terms of optimal design of the air cathode and electrolyte engineering. Finally, this review highlights the significance of reducing the polarization voltage to achieve the commercial application of metal–air batteries and looks forward to its broad prospects in the future energy storage field.

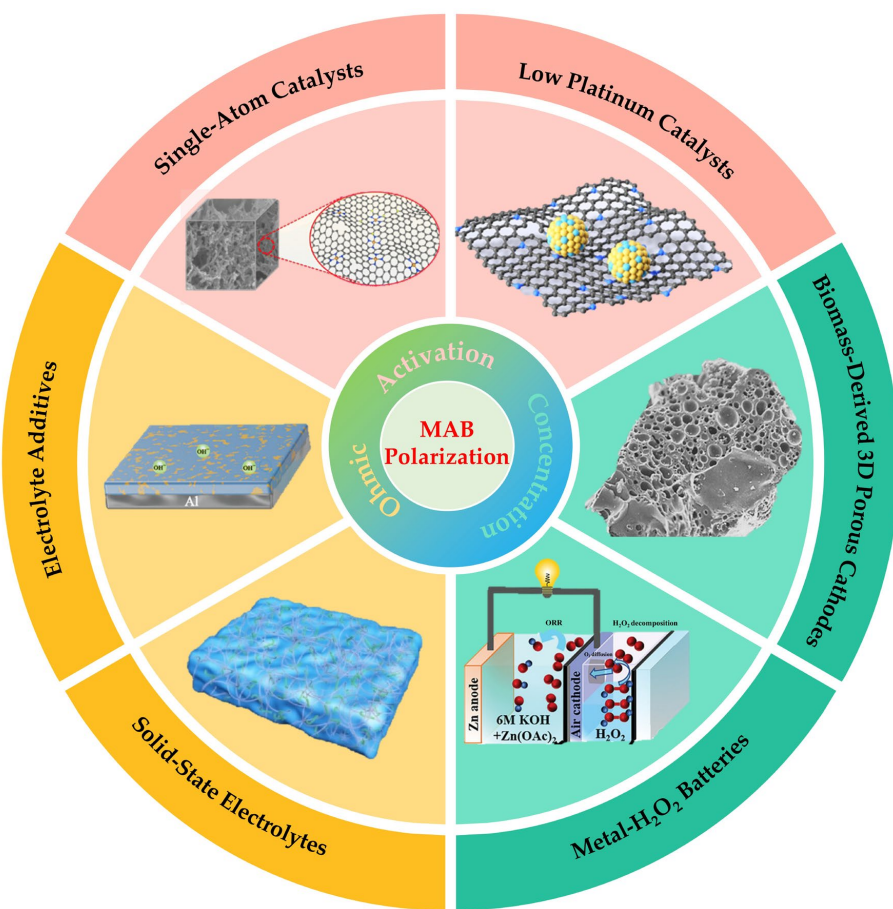


**Figure 2.** Battery polarization and corresponding response strategies for metal–air batteries (Adapted with permission from Ref. [23], The Royal Society of Chemistry 2024, Ref. [24], American Chemical Society 2024, Ref. [25] The Royal Society of Chemistry 2023, Ref. [26], John Wiley and Sons 2022, Ref. [27], John Wiley and Sons 2023, Ref. [28] John Wiley and Sons 2023.).

## 2. Working Mechanism and Battery Polarization Challenge of Metal–Air Batteries

### 2.1. Working Mechanism

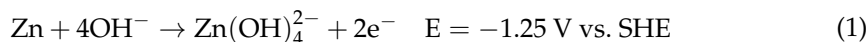
The metal–air battery is a kind of high-energy density electrochemical energy storage device that uses metal as the anode and air (oxygen) as the cathode active substance, with its core advantage being the use of oxygen in the air as the cathode reactant, which significantly reduces the mass of the battery and improves the energy density [29]. The basic structure of the metal–air battery consists of the metal anode, the air cathode, the electrolyte, and the diaphragm. The metal anode is usually made of active metals such as Zn, Li, Al, etc., and exists in the form of foil, powder, or porous structure, releasing electrons through oxidation reaction; the air cathode is a multi-layered design containing a gas diffusion layer (GDL), a catalytic layer, and a collector, in which the GDL composed of porous carbon-based materials allows oxygen to penetrate and prevents the leakage of the electrolyte, and the catalytic layer is loaded with precious metals or transition metal oxides to accelerate ORR and OER. The catalytic layer is composed of a catalyst, a binder, and a conductive agent. Both the binder and the conductive agent play indispensable auxiliary roles in the air cathode. The binder acts as the “framework” of the electrode structure, ensuring mechanical strength and porous structure and reducing concentration polarization to a certain extent; the conductive agent serves as the “wire network” inside the electrode, ensuring efficient electron transmission and reducing the internal resistance of the electrode. They work together to provide a stable, efficient, and durable reaction site and transmission path for oxygen reduction and oxygen evolution [30,31]. Therefore, while improving the catalyst activity, it is also necessary to select and study the most suitable binder/conductive agent combination and its optimization process. The collector is responsible for electron conduction. Depending on the system, the electrolyte is classified as aqueous (e.g., aqueous KOH solution [32]) or organic (e.g., Li salt dissolved in an ether solvent [33]), which provides an ion transport channel and participates in the electrochemical reaction; the diaphragm, usually made of porous polymer, prevents short-circuiting of the positive and negative electrodes while allowing free ion migration.

When the battery works, the anode of the metal is oxidized to release electrons, oxygen is reduced at the cathode and combined with ions in the electrolyte to form oxides, and the electrons pass through the external circuit to form an electric current, thus realizing the conversion of chemical energy into electrical energy. Due to the difference in electrolyte systems, the working principle of the aqueous metal–air battery and the organic metal–air battery is slightly different. For aqueous metal–air batteries (Zn–air battery, for example), the principle of operation revolves around the oxidation of Zn at the anode and the reduction of oxygen at the cathode [19]. During discharge, the Zn anode undergoes an oxidation reaction in an alkaline environment, generating  $Zn^{2+}$  ions (Equation (1)), which are further decomposed into Zn oxide and water (Equation (2)), and at the same time releasing electrons that flow through external circuits towards the cathode electrode [34]. On the cathode side of the air, oxygen flows through the porous carbon substrate material, forming a current through the porous carbon material, which is then converted into electrical energy. Oxygen diffuses through the porous carbon-based material to the catalytic layer, where it combines with water and electrons to undergo a reduction reaction in the presence of a catalyst, forming hydroxide ions to complete the charge transfer (Equation (3)). The total reaction throughout the discharge process is the formation of Zn oxide from Zn and oxygen at a theoretical voltage of approximately 1.65 V (Equation (4)) [34]. During charging, a voltage applied by an external power source forces the reaction to proceed in reverse: Zn oxide is reconverted to Zn in the alkaline electrolyte, while oxygen is released from the positive electrode (Equations (5)–(7)) [16,34]. However, passivation of the Zn negative

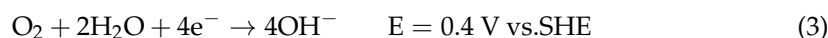
electrode (where the Zn oxide layer hinders the reaction), clogging of the electrode pores with carbonates generated by the electrolyte due to absorption of carbon dioxide from the air, and the growth of Zn dendrites during charging limit their cycle life. Despite the challenges, Zn–air batteries have been commercialized in low-power devices, such as hearing aids and sensors, due to their high theoretical energy density [9,21,35], low cost, and environmentally friendly properties, and continue to be optimized as a potential renewable energy storage solution [9,36].

#### Discharge process

##### Anode:



##### Air cathode:



##### Overall reaction:



#### Charging process

##### Anode:



##### Air cathode:



##### Overall charge reaction:



Al–air batteries, however, are mostly disposable batteries that need to be “mechanically recharged” by replacing the metal anode electrode [37]. In the discharge process of organic-based metal–air batteries represented by Li–air batteries, the Li anode loses electrons to be oxidized to Li ions, and the electrons are transferred to the anode through the external circuit (Equation (8)); oxygen diffuses through the porous structure of the anode to the catalytic layer, where it combines with the Li ions and the electrons to generate Li peroxide (Equation (9)) at a theoretical voltage of 2.96 V (Equation (10)). However, the electrolyte is susceptible to oxidative decomposition by superoxide radicals ( $\text{O}_2^-$ ), generating irreversible byproducts (e.g.,  $\text{Li}_2\text{CO}_3$  or  $\text{LiOH}$ ) that lead to capacity decay [17,34,38]. During charging, an external power supply is required to apply a high voltage (typically  $>4$  V) to force the decomposition of Li peroxide (Equation (11)), but this process is accompanied by intense oxidation of the electrolyte and growth of Li dendrites, which can lead to safety hazards [17,39]. In addition, dendrites generated on the surface of the Li anode may puncture the diaphragm and cause a short circuit, while  $\text{Li}_2\text{O}_2$  at the anode further reduces the reaction kinetics due to electrode passivation caused by the insulating properties [33,34,40]. To improve the performance, researchers have used bifunctional catalysts (e.g., bioenzymes [41]) to accelerate the oxygen reduction and precipitation reactions or have introduced solid-state electrolytes (e.g., ceramic oxides [42]) to inhibit the dendrites and widen the electrochemical window. Despite the remaining barriers to commercialization, Li–air batteries show transformative potential in long-range areas such as electric

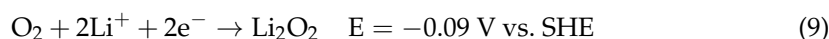
vehicles and drones, making them an important area to explore for the next generation of high-energy batteries.

Discharge process

Anode:



Air cathode:



Overall reaction:



Charging process



## 2.2. Battery Polarization Challenge

The performance of metal–air batteries is governed by a variety of polarization effects, mainly activation polarization, ohmic polarization, and concentration polarization, which together lead to the deviation of the actual battery voltage from the theoretical value, thus affecting the energy efficiency and power output [43]. Activation polarization arises from the retardation of the electrochemical reaction kinetics, in particular, the multi-step electron transfer processes of ORR and OER [44–46]. At very low current densities, the electrochemical reaction rate is slow, resulting in a very low consumption rate of oxygen on the electrode surface and a small concentration gradient. Meanwhile, due to the small current, the ohmic loss is also minimal. Under such circumstances, the main factor determining the drop in battery voltage is the overpotential required to overcome the activation energy barrier of the electrochemical reaction [44]. For rechargeable metal–air batteries, activation polarization will increase the charge–discharge voltage difference, leading to more energy loss [43]. Ohmic polarization, on the other hand, is caused by the internal resistance of the battery, including the low ionic conductivity of the electrolyte, the poor conductivity of the electrode materials, and the interfacial contact impedance [47]. Its effect grows linearly with the current density and manifests itself as a drop in the operating voltage [48], an accumulation of Joule heat [33], and a limitation of the power density [49,50]. Such polarization is exacerbated by a high-temperature or low-temperature environment. Concentration polarization is associated with insufficient substance transport rates, such as impeded cathode oxygen diffusion [51,52] and formation of local concentration gradients of metal ions at the anode or electrolyte mass transfer bottlenecks [53,54]. At high-rate discharges, the electrochemical reaction rate is extremely fast. The diffusion rate of reactants (especially oxygen at the cathode) to the active sites of the electrode cannot keep up with the consumption rate of the reaction, resulting in a sharp drop in the concentration of reactants on the electrode surface to nearly zero (the anode may also have problems with metal ion diffusion or product accumulation). At this point, in order to maintain a high reaction rate, a huge driving force is required to overcome the mass transfer limitation, and the concentration polarization overpotential increases sharply, becoming the most important factor for the voltage drop [21,55,56].

To mitigate the battery polarization effect, a multi-dimensional strategy is required. In order to address the activation polarization caused by the slow ORR and OER kinetics of air cathodes, the design of catalysts with bifunctional ORR/OER activity is an effective solution. Single-atom catalysts (SACs) and low platinum catalysts have been shown to exhibit excellent bifunctional activity and high utilisation of active sites. This has been

demonstrated to be an effective means of reducing the high overpotential caused by activation polarization, thus improving the cycle life of batteries. For metal–air batteries operating at high power, it is necessary to reduce the concentration polarization caused by insufficient oxygen diffusion under high current densities to maintain battery performance. Biomass-derived 3D cathode materials, with their high specific surface area and abundant pore structures, provide more three-phase reaction interfaces for ORR/OER and significantly promote oxygen diffusion; in addition, optimizing battery structures such as metal–H<sub>2</sub>O<sub>2</sub> batteries can increase the oxygen concentration on the cathode side and accelerate oxygen diffusion, thereby indirectly suppressing concentration polarization. Regarding ohmic polarization, in addition to the rational design of the cathode catalytic layer, it is currently more important to protect the metal anode to inhibit its self-corrosion and passivation, thereby reducing the internal resistance of the electrode. The development of electrolyte additives to form protective coatings on metal anodes and the design of solid electrolytes can effectively inhibit anode self-corrosion and passivation caused by the accumulation of reaction products, reducing the additional power loss caused by ohmic polarization. The synergistic improvement of materials, structures, and processes can effectively suppress the polarization phenomenon and promote the practical application of these batteries in the field of high-energy storage and power.

### 3. Air Cathode Optimized Design

#### 3.1. Single-Atom Catalysts (SACs)

Single-atom catalysts (SACs) achieve atomic-level dispersion of active sites by anchoring isolated metal atoms to the carrier surface, thus breaking through the limitations of traditional nanoparticle catalysts in terms of atom utilization and interfacial synergistic effects [57–60] since the first report of Pt<sub>1</sub>/FeO<sub>x</sub> catalysts and the introduction of the concept of “single-atom catalysis” by Tao Zhang’s team in 2011 [61]. In Table 1, we summarize some of the SACs published in recent years; these catalysts have been characterized by their unique electronic structure (e.g., unsaturated coordination environments, quantum size effect) and nearly 100% metal atom utilization, with highly dispersed 3D transition metal–nitrogen ligand fraction (often considered to be the active center for adsorption of O<sub>2</sub> molecules and catalysis of ORR/OER) [5,62].

**Table 1.** Previously reported electrocatalytic and Zn–air battery performance of SACs.

Catalyst	E <sub>1/2</sub> (V vs. RHE)	E <sub>10</sub> (V vs. RHE)	OCV (V)	P <sub>max</sub> (mW cm <sup>-2</sup> )	Cycling (h/mA cm <sup>-2</sup> )	Ref.
VMoON@NC	0.861	1.417	1.392	376.4	>630/10	[57]
Fe-N <sub>x</sub> -C	0.91	1.83	1.51	96.4	300/5	[63]
FeN <sub>4</sub> /NGO	0.91	-	-	217	100/10	[64]
Fe-Z8NC&NaCl	0.896	-	1.52	104	>100/20	[65]
Fe-NNCv	0.924	1.64	1.57	99.1	>330/10	[66]
g-Cu-SACs	0.92	-	1.48	112	>650/5	[67]
Fe-N <sub>x</sub> @NSCST-ZL	0.94	1.71	1.47	196.21	>750/5	[68]
Fes <sub>a</sub> /N,S-PHLC	0.91	-	1.47	217	>882/5	[69]
FeN-SC	0.92	-	1.46	251	140/10	[70]
Fe <sub>1</sub> /NCP	0.95	1.6	1.50	263.8	350/10	[71]
Fe <sub>3</sub> C@NCNTs	0.84	-	1.61	194	>100/10	[72]
FeS/Fe <sub>3</sub> C@Fe-N-C	0.91	1.506	1.432	113	>24/50	[73]
FAS-NSC@950	0.871	1.544	1.48	181.8	>72/10	[74]
Fe <sub>3</sub> Co <sub>7</sub> -NC	0.893	1.573	-	133	>400/2	[75]
FeCu SACs@NSC	0.89	1.68	1.47	152	>300/5	[76]
FeMn-DSAC	0.922	1.635	1.45	184	>80/2	[77]
FeNi-DSAs-PNCH	0.89	-	1.48	99.20	-	[78]
FeZn-NC-800	0.89	-	1.508	218.6	>200/10	[79]
FeCoCuZn-SACs	0.89 V	1.51	1.51	252	>225/5 and 10	[80]

Han et al. reported an efficient single-atom Fe-N<sub>x</sub>-C electrocatalyst [63]. The Fe atoms of the catalyst were uniformly dispersed on the nitrogen-doped carbon skeleton in the form of single atoms to form stable Fe-N<sub>x</sub> active sites, and the rigid nanocage structure of ZIF-8 effectively inhibited the agglomeration of Fe atoms during the pyrolysis process. The application of Fe-N<sub>x</sub>-C in Zn-air batteries resulted in an open circuit voltage (OCV) as high as 1.51 V and a power density of 96.4 mW cm<sup>-2</sup>. These performance advantages stem from the high active site utilization of the single-atom structure and the stability of the carbon skeleton, which effectively reduces the ORR/OER overpotential while suppressing Zn anode side reactions. The additive-assisted pyrolysis strategy demonstrated significant advantages in the preparation of SACs [81]. Cao et al. disrupted the chemical bonding of bulk Fe<sub>2</sub>O<sub>3</sub> by the strong polar effect of molten NaCl at high temperatures, which induced the volatilization of the Fe species and their anchoring to the ZIF-8-derived nitrogen-doped porous carbon carriers, resulting in the formation of atomically dispersed Fe-N<sub>4</sub>-O<sub>2</sub> active sites (Figure 3a) [65]. XANES and EXAFS analysis confirmed the local coordination environment of Fe-N<sub>4</sub>-O<sub>2</sub> (Figure 3b,c). The Fe atoms were coordinated to nitrogen in the Fe<sup>2+</sup>/Fe<sup>3+</sup> valence state, which was shown to form a stable single-atomic configuration by HAADF-STEM (Figure 3d). Thanks to the unique single-atom active site and optimized electronic structure, Fe-Z8NC&NaCl exhibited excellent ORR performance in 0.1 M KOH, with a half-wave potential (0.896 V vs. RHE) and kinetic current density (36.1 mA cm<sup>-2</sup>) superior to that of commercial Pt/C (0.85 V, 6.4 mA cm<sup>-2</sup>) (Figure 3e). The Fe-Z8NC&NaCl cathode assembled Zn-air battery exhibited a high OCV of 1.52 V and a peak power density ( $P_{max}$ ) of 104 mW cm<sup>-2</sup> (Figure 3f,g). Sun prepared Fe SACs (Fe-NNCv) by a “post-adsorption–secondary pyrolysis” strategy combined with melamine (MA) etching [66]. By introducing MA molecules into the precursor ZIF-8, the particle size was significantly reduced to about 46 nm, and the decomposition and volatilization of MA during high-temperature pyrolysis were utilized to introduce abundant carbon vacancies in the carbon matrix. Due to the abundance of vacancies generated by the high-temperature volatile etching of MA, Fe-NNCv exhibits an excellent half-wave potential (0.924 V vs. RHE) in 0.1 M KOH and no performance degradation after 5000 cycles. The Fe-NNCv Zn-air battery exhibits a high OCV of 1.57 V and a peak power density of 99.1 mW cm<sup>-2</sup> with a cycle stability of more than 330 h.

Compared with the conventional gradual warming pyrolysis method, a very short thermal treatment time seems to be effective for the synthesis of nanocomposites containing small molecules [82]. Fei et al. successfully synthesised SACs by the ultrafast heating effect of microwaves [82,83]. This rapid heating process prevents metal agglomeration and thus reduces the amount of catalyst used. The transient heat treatment-based Fe single atomic catalyst FeN<sub>4</sub>/NGO utilizes CO generated from the decomposition of DMF to repair carbon vacancy defects in graphene, which promotes the anchoring of Fe atoms on the surface of nitrogen-doped graphene and the formation of a stable Fe-N<sub>4</sub> coordination configuration via oxygen bridges [64]. The FeN<sub>4</sub>/NGO cathode exhibited a peak power density of 217 mW cm<sup>-2</sup>, 40% improvement over Pt/C, and achieved a high specific capacity of 750 mA h g<sup>-1</sup>. This performance advantage stems from the synergistic optimization of active site density, electronic structure, and carrier stability by the transient thermal treatment strategy.

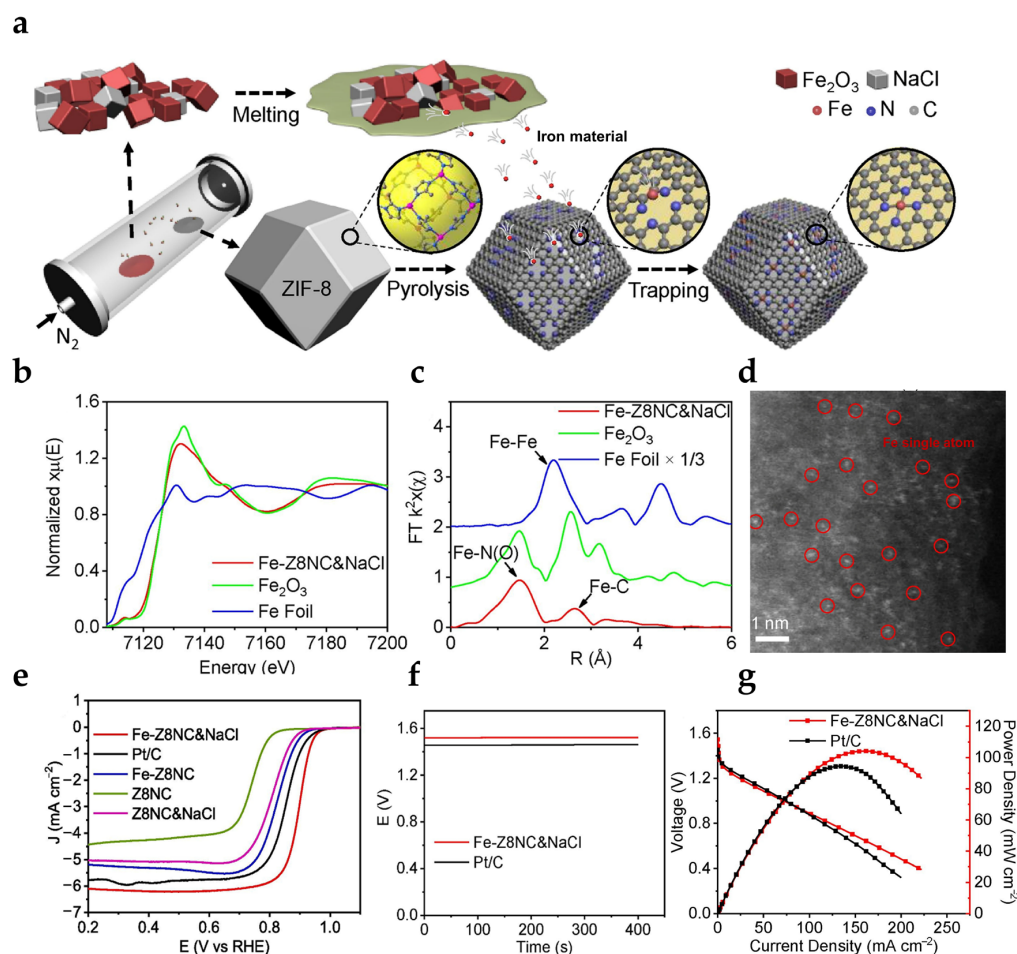


**Figure 3.** (a) Schematic illustration of the preparation of Fe-Z8NC&NaCl via the salt-assisted emitting approach; (b) Fe K-edge X-Ray absorption near-edge structure XANES spectra and (c) Fe K-edge k<sup>2</sup>-weighted Fourier transform (FT)-EXAFS spectra of Fe-Z8NC&NaCl,  $\text{Fe}_2\text{O}_3$ , and Fe foil, respectively; (d) the magnified aberration-corrected HAADF-STEM image of Fe-Z8NC&NaCl catalyst; (e) the iR-corrected polarization curves at 1600 rpm; (f) open-circuit potential of Fe-Z8NC&NaCl-based and 20% Pt/C-based Zn-air batteries; (g) polarization and power density curves of Fe-Z8NC&NaCl-based and 20% Pt/C-based Zn-air batteries (Adapted with permission from Ref. [65], Elsevier 2021.).

However, the symmetric M-N coordination structure of conventional SACs generally suffers from the intrinsic defect of excessively high intermediate adsorption energy barriers during oxygen electrocatalysis [84,85]. To address this kinetic bottleneck, recent studies have shown that the electronic structure properties of the active center can be precisely regulated by introducing second heteroatoms such as S [23,86,87], B [88], P [71], Cl [89], or nanoparticles (e.g., metal particles [90–92], FeS [74],  $\text{Fe}_3\text{C}$  [72]) for coordination microenvironmental modulation. On the one hand, the electron absorbing/supplying capacity of the metal center can be altered to optimize the strength of intermediate adsorption; on the other hand, an asymmetric charge distribution is induced to enhance the orbital hybridization between the catalytic site and the oxygen intermediate ( $^*\text{OOH}/^*\text{O}$ ), which significantly improves the catalytic reaction kinetics of SACs [71]. Yang et al. prepared ultrathin mesoporous N/S co-doped graphene substrates via KSCN-assisted pyrolysis of ZIF-8 and used a volatilization-trapping strategy to anchor Cu single atomic sites [67]. The resulting Zn-air batteries assembled with g-Cu-SACs exhibited a peak power density of  $112 \text{ mW cm}^{-2}$  and maintained a stable charge/discharge voltage difference ( $\Delta V < 0.85 \text{ V}$ ) over 650 h of cycling.

Zhang et al. [70] prepared FeSN-C with sulphur atoms located in the first coordination shell layer and FeN-SC with sulfur atoms located in the second coordination shell layer (Figure 4a). The sulfur atoms in FeN-SC are distributed in the secondary coordination layer of the Fe active center by indirect coordination to form a unique Fe-N-S configuration, while sulfur atoms in FeSN-C are directly involved in the formation of Fe-S bonds in the first coordination layer of Fe (Figure 4b,c). The sulfur in the second coordination shell layer modulates the charge density of the Fe center through the long-range electronic effect to optimize the Gibbs free energy of the  $^{*}\text{OH}$  desorption step ( $\Delta G = 0.37 \text{ eV}$ ), breaking through the activity bottleneck of the conventional  $\text{Fe}-\text{N}_4$  symmetric structure. The Zn–air battery assembled based on FeN-SC exhibited a peak power density of  $251 \text{ mW cm}^{-2}$  (Figure 4d).

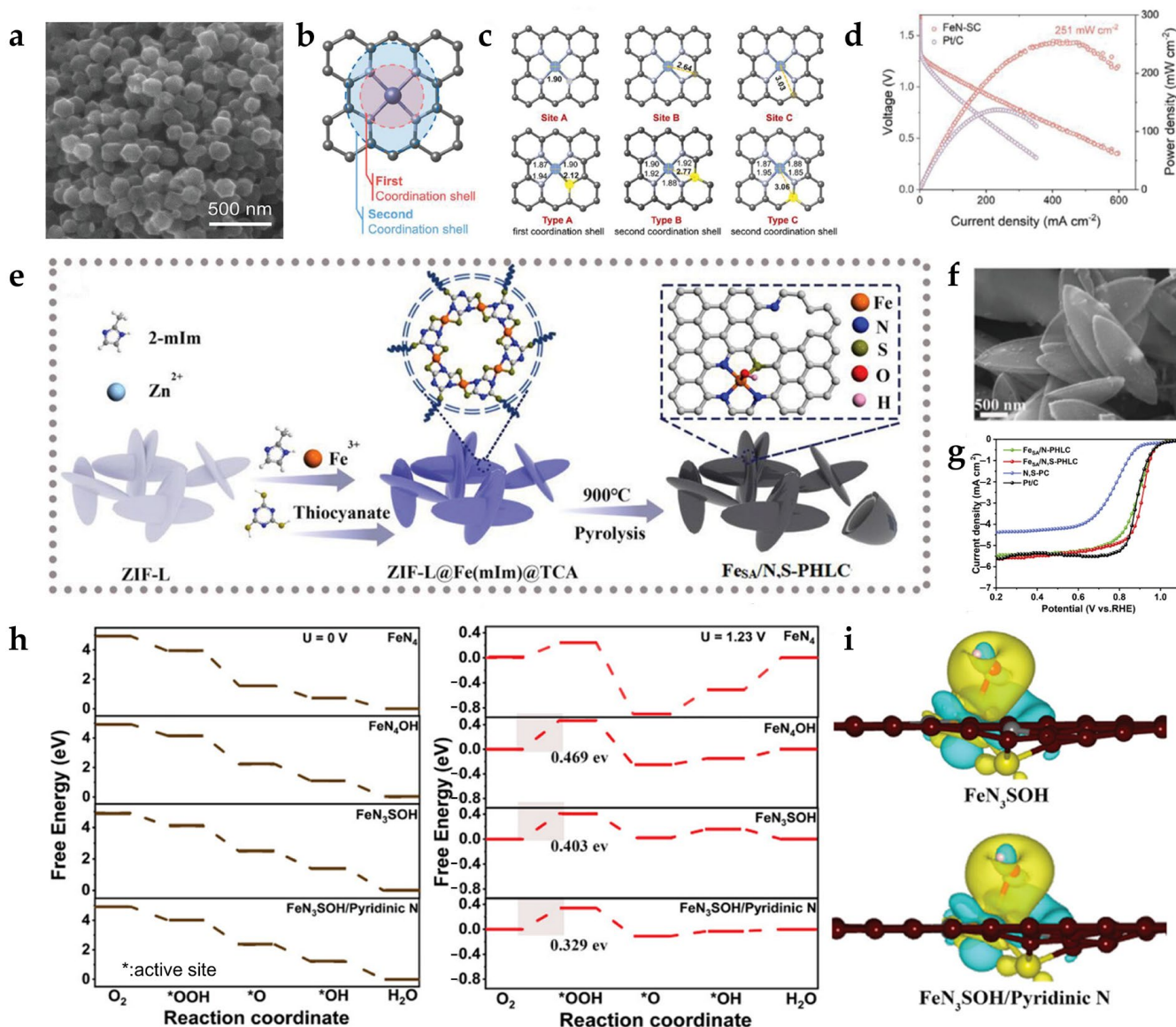


**Figure 4.** (a) SEM image of FeN-SC catalyst; (b) schematic diagram of coordination shell and (c) the distances from the atoms to the center of the Fe atom (unit: Å); (d) polarization and power density curves, reproduced by permission [70]; (e) Roadmap for  $\text{Fe}_{\text{SA}}/\text{N},\text{S}$ -PHLC preparation; (f) SEM of  $\text{Fe}_{\text{SA}}/\text{N},\text{S}$ -PHLC; (g) LSV curves of  $\text{Fe}_{\text{SA}}/\text{N},\text{S}$ -PHLC,  $\text{Fe}_{\text{SA}}/\text{N}$ -PHLC, Pt/C, and N,S-PC samples in 0.1 M KOH solution; (h) Gibbs free energy diagram of ORR at  $U = 0 \text{ V}$  and  $U = 1.23 \text{ V}$ ; (i) differential charge density of  $\text{FeN}_3\text{SOH}$  and  $\text{FeN}_3\text{SOH}/\text{Pyridinic N}$  (Adapted with permission from Ref. [69], John Wiley and Sons 2024.).

Li et al. reported a Fe SAC ( $\text{Fe-N}_x@\text{NSCST-ZL}$ ) prepared based on a two-dimensional blade-like ZIF-L template, in which Fe single atoms were anchored to N/S co-doped carbon nanosheets/carbon nanotubes [68]. Using sulfate as the sulfur source,  $\text{Fe-N}_x@\text{NSCST-ZL}$  formed thiophene sulfur (C-S-C) and induced carbon skeleton defects during pyrolysis while retaining the two-dimensional layered structure of ZIF-L.  $\text{Fe-N}_x@\text{NSCST-ZL}$  constructed a multi-stage pore system with a high specific surface area, where the *in situ* generated carbon nanotubes significantly enhanced the electron conduction and mass transfer efficiency. Yuan et al. further constructed active centers with  $\text{FeN}_3\text{SOH}$  five-coordination structures on nitrogen–sulfur co-doped porous hollow blade carbon substrates by a host-dual-guest sulfide-assisted strategy [69]. The two-dimensional ZIF-L was used as the host template in the synthesis process.  $\text{Fe}_{\text{SA}}/\text{N,S-PHLC}$  with a double-shell layer hollow blade structure realized the modulation of the iron coordination environment by sulfur atoms (Figure 4e,f). The unique double-shell layer hollow structure not only retains the high specific surface area property of ZIF-L but also its rich mesoporous structure (with a specific surface area of  $848.94 \text{ m}^2 \text{ g}^{-1}$ ), and sulfur doping-induced defective sites significantly enhance the exposure degree of the active sites and the material transport efficiency. XAFS analysis confirms that Fe exists in an atomically dispersed  $\text{FeN}_3\text{SOH}$  configuration, in which axial hydroxyl coordination and planar asymmetric N/S coordination synergistically optimize the 3D-orbital electronic structure of Fe (Figure 4i), and Figure 4h showed such a unique coordination environment significantly reduces the energy barrier of  ${}^*\text{O}\rightarrow{}^*\text{OOH}$  by modulating the adsorption energy barrier of the oxygen intermediate (theoretical calculations show an overpotential of 0.329 eV).  $\text{Fe}_{\text{SA}}/\text{N,S-PHLC}$  exhibited a half-wave potential of 0.91 V (vs. RHE) in 0.1 M KOH (Figure 4g) and also reached 0.75 V (vs. RHE) under acidic conditions. When applied to Zn-air batteries, the structure–performance synergistic effect of  $\text{Fe}_{\text{SA}}/\text{N,S-PHLC}$  enables the Zn-air batteries to obtain an OCV of 1.47 V and a peak power density of  $217 \text{ mW cm}^{-2}$ . The stable coordination structure of the  $\text{FeN}_3\text{SOH}$  active center and the good mechanical stability of the carbon carrier together supported a cycle life of up to 882 h. Sun et al. reported a carbon-based Fe SAC ( $\text{FeS}/\text{Fe}_3\text{C}@/\text{Fe-N-C}$ ) prepared by a one-step pyrolysis method [73]. Its half-wave potential in 0.1 M KOH electrolyte reached 0.91 V (vs. RHE). Meanwhile, the overpotential ( $E_{10}$ ) of the OER in 1 M KOH is 1.506 V (vs. RHE), which is comparable to that of  $\text{RuO}_2$  (1.518 V). Attributed to the modulation of the electron distribution at the  $\text{Fe-N}_4$  site by  $\text{FeS}/\text{Fe}_3\text{C}$  nanoparticles and the charge transport facilitated by the highly graphitized carbon layer, the liquid Zn-air battery assembled with  $\text{FeS}/\text{Fe}_3\text{C}@/\text{Fe-N-C}$  exhibited a peak power density of  $113 \text{ mW cm}^{-2}$ , which was superior to that of the  $\text{Pt/C+RuO}_2$  system.

Recently, it has been shown that the catalytic performance of ORR/OER can be significantly enhanced by introducing a second metal atom into SACs to construct a dual-atom catalyst system [77,93]. The enhancement of the catalytic performance is attributed to three key mechanisms: the effective regulation of the electronic structure of the active sites, the optimal modulation of the adsorption behaviour of oxygen intermediates by heterogeneous metal atoms, and the synergistic effect between the active sites of different metals [76,94,95]. In particular, the electronic interactions between heterogeneous atoms not only improve the binding energy of the reaction intermediates but also form more favorable catalytically active centers through geometrical restructuring [76]. Fe-Co dual single atomic catalysts (FeCo-NC) were prepared by a synergistic hydrothermal–pyrolysis strategy by Gu et al. [75] FeCo-NC retained the dodecahedral structure of ZIF-8 (Figure 5a,b) and was based on atomically dispersed  $\text{Fe-N}_4$  and  $\text{Co-N}_4$  sites as active centers, and the coexistence of adjacent Fe/Co double sites (spacing  $\sim 3.4 \text{ \AA}$ ) was observed by AC-HAADF-STEM (Figure 5c,d). XANES and EXAFS analyses confirmed that both Fe/Co are in the +1~+2 valence states, forming a tetra-coordinated structure that is strongly coupled to the carbon matrix. This

two-site synergistic effect enabled  $\text{Fe}_3\text{Co}_7\text{-NC}$  to exhibit a half-wave potential up to 0.893 V (vs RHE) in 0.1 M KOH, and the tafel slope was as low as 42 mV dec<sup>-1</sup>, indicating faster reaction kinetics; the overpotential at 10 mA cm<sup>-2</sup> was only 343 mV, lower than that of RuO<sub>2</sub> (402 mV). Flexible solid-state Zn-air batteries assembled based on FeCo-NC have higher discharge plateaus and smaller charge/discharge voltage gaps at high current densities and have a long cycling stability of more than 400 h (Figure 5e).

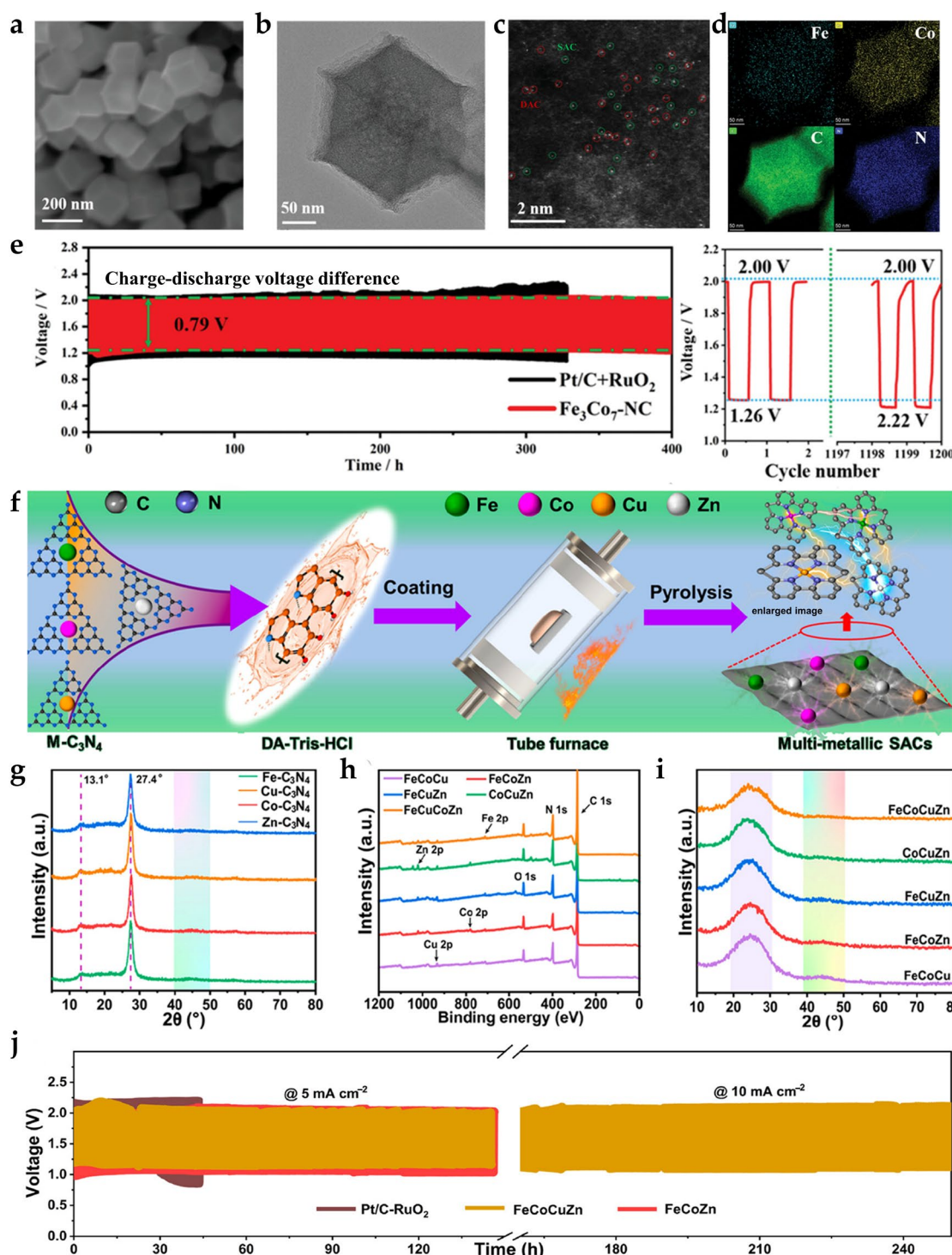


**Figure 5.** (a) SEM, (b) TEM, (c) HAADF-STEM, and (d) EDS elemental mapping images of  $\text{Fe}_3\text{Co}_7\text{-NC}$ ; (e) galvanostatic cycling stability at 2 mA cm<sup>-2</sup> of ZAB- $\text{Fe}_3\text{Co}_7\text{-NC}$  and ZAB-Pt/C+RuO<sub>2</sub> at 30 °C, and magnified plots of the galvanostatic discharge and charge curves at different cycling stages for ZAB- $\text{Fe}_3\text{Co}_7\text{-NC}$  at 30 °C (Adapted with permission from Ref. [75], John Wiley and Sons 2022.).

(f) Schematic illustration of synthesizing MM-SACs supported on NC, including trimetallic FeCoCu-SACs, FeCoZn-SACs, FeCuZn-SACs, CoCuZn-SACs, and quatermetallic FeCoCuZn-SACs; (g) XRD patterns of M-C<sub>3</sub>N<sub>4</sub> as precursors; (h) survey XPS spectra and (i) XRD patterns of MM-SACs; (j) galvanostatic discharging and charging curves at 5 and 10 mA cm<sup>-2</sup> (Adapted with permission from Ref. [80], John Wiley and Sons 2022.).

Wang et al. synthesized FeNi bimetallic SACs (FeNi-DSAs-PNCH) [78]. Fe and Ni were anchored to the carbon skeleton in the form of single atoms to form Fe-N<sub>x</sub> and Ni-N<sub>x</sub> active sites. The adjacent Ni-N<sub>x</sub> sites optimized the adsorption-desorption equilibrium of oxygen intermediates by modulating the d-band center of the Fe-N<sub>x</sub> sites, which significantly enhanced the catalytic activity. In a 0.1 M KOH electrolyte, FeNi-DSAs-PNCH exhibits a half-wave potential of 0.89 V (vs. RHE), and the current density is maintained at 96% after 26,000 s of continuous operation. The enhancement of ORR and OER catalytic performance of SACs by doping with polynmetallic elements has been reported [96]. Li et al. prepared trimetallic (e.g., FeCoZn, FeCuZn) and quatermetallic (FeCoCuZn) single-atom catalysts (Figure 5f) [80]. The catalysts were based on ultrathin nitrogen-doped carbon, and the metals were uniformly dispersed in the form of isolated single atoms. The absence of Fe, Co, Cu, and Zn metal characteristic peaks was confirmed by XRD and XPS analysis (Figure 5g–i). The XPS analyses showed that the metals formed a coordination structure with nitrogen (M-N<sub>x</sub>), and there were significant electronic interactions among the multimetals (e.g., Fe 2p binding energy positively shifted and Cu 2p negatively shifted) that synergistically regulate the electronic structure of the active site. The quatermetallic FeCoCuZn-SACs exhibited a half-wave potential of up to 0.89 V (vs RHE) in 0.1 M KOH, a kinetic current density (14.20 mA cm<sup>-2</sup> @0.85 V), and an overpotential of 280 mV at 10 mA cm<sup>-2</sup>. The FeCoCuZn-SACs assembled Zn-air battery exhibited an OCV of 1.51 V and a specific capacity of 817 mA h g<sup>-1</sup> (close to the theoretical value of 820 mA h g<sup>-1</sup>). In the charge-discharge cycling test, the catalyst demonstrated excellent cycling durability with a voltage gap increase of only 0.78 V after 145 h of operation at 5 mA cm<sup>-2</sup> and another 80 h of stable operation at 10 mA cm<sup>-2</sup> (Figure 5j).

### 3.2. Low Platinum Catalysts

Platinum (Pt) is still the material of choice for ORR due to its excellent catalytic activity and stability, but high Pt loading (10–20%) leads to a high cost of the electrocatalyst [97,98]. In addition, Pt nanoparticles are prone to agglomeration and detachment during long-term operation, with a significant decrease in catalytic activity and lifetime [24]. Therefore, to reduce the Pt content as well as the cost and improve the catalytic efficiency of electrocatalysts, researchers have developed a variety of Pt-based alloy compounds or bimetallic nanostructures for ORR [99,100]. Li et al. prepared nitrogen-doped carbon-loaded PtSn alloy nanocatalysts (PtSn/NC) by a synergistic strategy of electroless deposition and carbothermal reduction [24]. The Zn-air battery assembled based on the PtSn/NC catalyst exhibited excellent performance with a peak power density of 150.1 mW cm<sup>-2</sup> at a low Pt loading (20 µg·cm<sup>-2</sup>). Yang et al. reported a low platinum-loaded electrocatalyst (PtCoCN(CDs-X)) based on carbon dots (CDs) doped ZIF-67 derivatives (Figure 6a) [101]. CDs were first introduced into the ZIF-67 framework to form a cobalt nanoparticle-coated nitrogen-doped carbon carrier (CoCN) (CDs-X), which was subsequently anchored with Pt nanoparticles on the surface by chemical reduction (Pt loading <5 wt.%). The CDs optimised the Pt-carrier interactions through the formation of Co-O bonds, promoting the formation of PtCo alloys. The optimized PtCoCN (CDs-0.10) assembled Zn-air battery reached a peak power density of 194.2 mW cm<sup>-2</sup>.

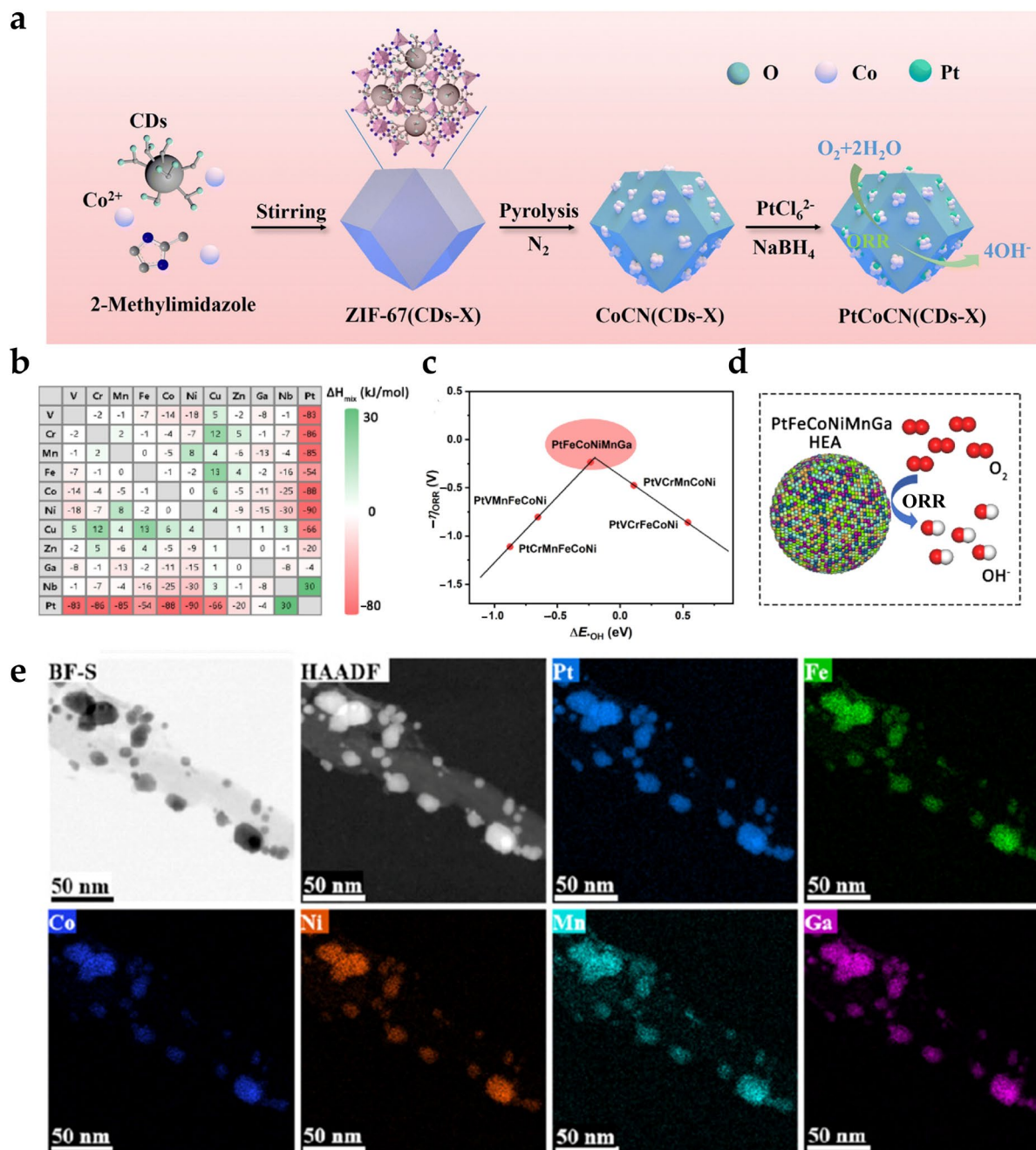


**Figure 6.** (a) Schematic illustration of the formation of the PtCoCN(CDs-X) catalyst (Adapted with permission from Ref. [101], The Royal Society of Chemistry 2024.); (b) enthalpy of mixing between two of the selected elements; (c) theoretical calculation of ORR properties of relevant Pt-based alloys with VEC  $\geq$  8; (d) schematic diagram of catalytic mechanism of oxygen reduction reaction of PtFeCoNiMnGa HEA nanoparticles; (e) EDS mapping graph of PtFeCoNiMnGa/CNT (Adapted with permission from Ref. [102], Elsevier 2024.).

Zhong et al. successfully prepared PtFeNC by stepwise introduction of Fe and Pt species into the ZIF-8 framework [100]. Attributed to the Pt–Fe dual-site synergistic promotion of O<sub>2</sub> dissociation and the optimization of intermediate product adsorption–desorption energy barriers, the Zn–air batteries assembled based on PtFeNC exhibit an OCV of 1.492 V and a peak power density as high as 148 mW cm<sup>-2</sup>. Among all metallic elements, the  $\Delta H_{\text{mix}}$  values for atomic combinations of platinum with other elements are below the upper safety limit, which means that platinum can be more easily alloyed with other elements without phase separation (Figure 6b) [103]. Taking advantage of this property

of the platinum element, Luo et al. predicted the catalytic performance of the five most promising six-element platinum-based high entropy alloys by DFT calculations (Figure 6c) and finally chose PtFeCoNiMnGa (Figure 6d) [102]. The high entropy phase structure was fixed by ultrafast quenching in liquid nitrogen, and the PtFeCoNiMnGa nanoparticles were finally obtained as homogeneously loaded on the surface of the CNTs (Figure 6e). The PtFeCoNiMnGa/CNT has a low overpotential of 243 mV in 1 M KOH and a mass activity of  $1.12 \text{ A mg}_{\text{Pt}}^{-1}$  (0.9 V vs. RHE) in the ORR test (0.1 M KOH), which is 5.3 times higher than that of Pt/C. Due to the high entropy phase inhibition of elemental segregation and enhanced structural stability of the CNT carrier, the OER/ORR activities were maintained at 87% and 95% respectively, after 50 h of constant-current testing. The Zn-air battery assembled based on this catalyst exhibits an OCV of 1.52 V and a peak power density of  $130.6 \text{ mW cm}^{-2}$ .

### 3.3. Biomass-Derived 3D Porous Cathodes

The ORR/OER catalytic process in metal–air batteries occurs at a complex three-phase interface (gaseous feedstock/liquid electrolyte/solid cathode) [104,105]. Therefore, a well-designed 3D porous cathode catalyst structure can effectively promote the oxygen diffusion and ORR/OER process [106–108]. Our group achieved the synergistic construction of in situ-grown 1D nitrogen-doped carbon nanotubes and 2D porous carbon nanosheets [109]. The unique 3D structure combines the high electrical conductivity and ion diffusion channel advantages of 1D carbon nanotubes with the high specific surface area and loading capacity of 2D nanosheets, which effectively promotes oxygen diffusion and inhibits the agglomeration of active sites. Excellent ORR performance was demonstrated under 0.1 M KOH alkaline conditions ( $E_{1/2} = 0.87 \text{ V}$ ). The peak power density of the assembled Zn–air battery reached  $294 \text{ mW cm}^{-2}$ .

Recently, some biomass materials have been reported as high-performance ORR/OER catalysts due to their natural porous structure and low-cost advantage, such as wood [110,111], corn [112], chitosan [113], soybean [114,115], and algae [116,117]. In Table 2, biomass-derived catalysts exhibit excellent bifunctional catalytic activity for both ORR and OER. Moreover, its high specific surface area and porous characteristics effectively promote oxygen diffusion, thereby enabling high-power-density zinc–air batteries. Jiao et al. reported a high-density Fe SAC (Fe SA/NCZ) prepared from corn silk as a biomass precursor, where 4.3 wt.% Fe single atom loading and 10 wt.% ultrahigh nitrogen doping are successfully achieved. Fe SA/NCZ exhibits a unique hierarchical porous tubular structure, with micropores providing single atom anchoring sites, and meso- and macropores facilitating oxygen diffusion and electron transport to form a highly efficient three-phase reactive interface [118]. Jiang et al. successfully constructed  $\text{Co}_3\text{Fe}_7\text{-Fe}_3\text{C}$  heterostructures by using soybean roots as a carbon source [115]. The  $\text{Co}_3\text{Fe}_7\text{-Fe}_3\text{C}$  heterostructure has a unique 3D honeycomb porous carbon skeleton inherited from the layered channel structure of soybean roots, while a heterojunction with strong electronic interactions is formed through the interfacial coupling of  $\text{Co}_3\text{Fe}_7$  alloy with  $\text{Fe}_3\text{C}$ . The assembled Al–air battery achieved a peak power density of  $210 \text{ mW cm}^{-2}$ . By mechanically replacing the Al anode, the battery has been continuously discharged at  $100 \text{ mA cm}^{-2}$  for 70 h, demonstrating excellent cycling stability. Algae can be enriched with large amounts of nutrients (nitrogen and phosphorus) from the environment and have a rich pore structure, making it a favorable and viable method of converting algae into an air cathode for metal–air batteries [116]. Our group uses a nori single-cell layer as a macroporous template and utilizes its natural microcellular array structure to adsorb  $\text{Co}^{2+}$  ions and generate ZIF-67 precursor in situ via 2-methylimidazole [25]. ZIF-67/nori-800 was activated by KOH to form a hierarchical porous structure with macropores ( $0.2\text{--}2 \mu\text{m}$ ), mesopores ( $2\text{--}12 \text{ nm}$ ), and micropores ( $0.5\text{--}2 \text{ nm}$ ) with a hierarchical porous structure and high specific surface

area ( $1454.3 \text{ m}^2 \text{ g}^{-1}$ ) (Figure 7a–d). ZIF-67/nori-800 demonstrated outstanding bifunctional catalytic activity. Its ORR half-wave potential in 0.1 M KOH reached 0.85 V (vs. RHE), surpassing that of commercial Pt/C. Furthermore, for OER in 1 M KOH, ZIF-67/nori-800 achieved a low overpotential of 230 mV, significantly outperforming RuO<sub>2</sub> (363 mV).

**Table 2.** Previously reported ORR/OER and Zn-air battery performance of biomass-derived catalysts.

Catalyst	Specific Surface Area ( $\text{m}^2 \text{ g}^{-1}$ )	$E_{1/2}$ (V vs. RHE)	$E_{10}$ (V vs. RHE)	$P_{\max}$ ( $\text{mW cm}^{-2}$ )	Ref.
Fe SA/NCZ	912	0.87	1.55	101	[118]
RN350-Z(1-2)-1000	1835	0.868		204	[114]
SV-900	464.94	0.822	1.56	732.77	[119]
SA-FeCNS-800	1192	0.85	1.615	209	[111]
MPWC-FeSA	454	0.85		152	[110]
N/biochar-800-7	1334	0.9		125	[117]
ZIF-67/nori-800	1454.3	0.85	1.46	476	[25]
CoN-BC-0.3	273.6	0.83	1.55	226	[120]
ZnCo-NC-S-900	279.5	0.90	1.57	510	[121]

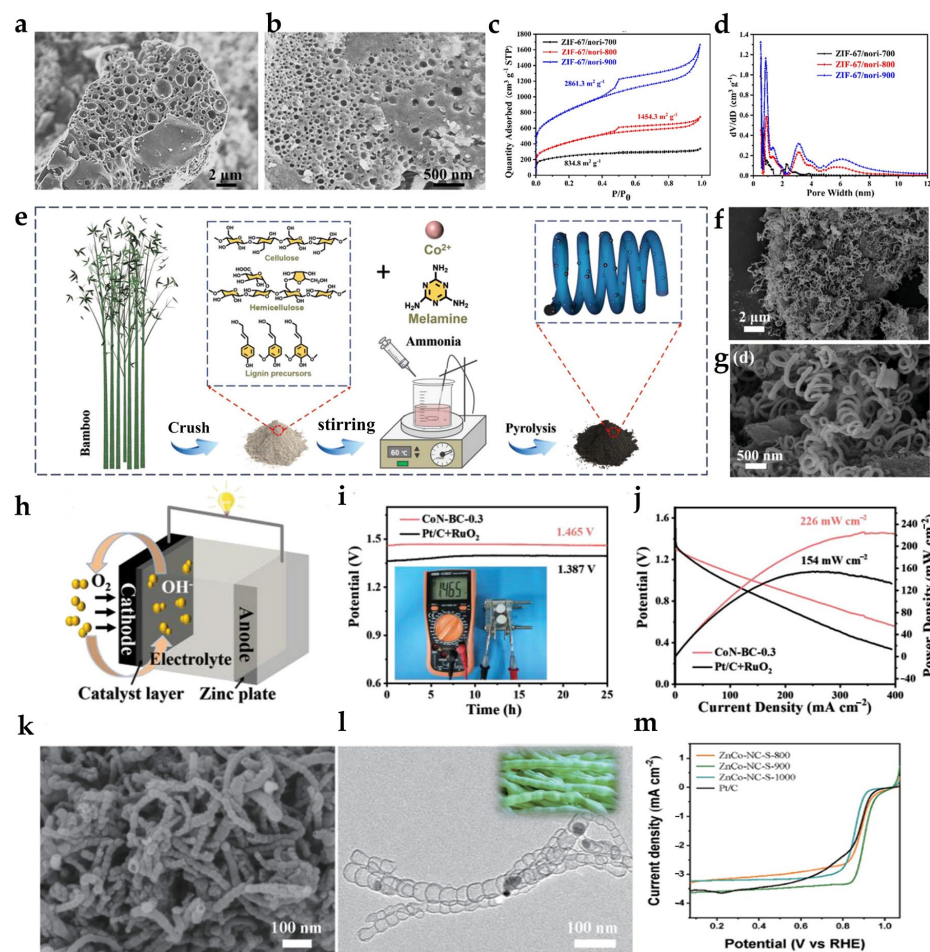


**Figure 7.** (a,b) FESEM of ZIF-67/nori-800; (c)  $\text{N}_2$  adsorption–desorption isotherms and (d) the pore size distributions of ZIF-67/nori-derived catalysts (Adapted with permission from Ref. [25], The Royal Society of Chemistry 2023.); (e) Schematic illustration for the synthesis of CoN-BC-0.3; (f,g) SEM images of CoN-BC-0.3; (h) schematic illustration of aqueous ZABs; (i) open-circuit plots of ZABs based on CoN-BC-0.3 and 20% Pt/C+RuO<sub>2</sub>; (j) discharge polarization curves and corresponding power densities of ZABs based on CoN-BC-0.3 and 20% Pt/C+RuO<sub>2</sub> (Adapted with permission from Ref. [120] John Wiley and Sons 2023.); (k) FESEM image and (l) TEM of the optimized catalyst (ZnCo-NC-S-900); (m) LSV curves (Adapted with permission from Ref. [121], Springer Nature 2024.).

Chen et al. prepared a helical carbon nanotube-encapsulated cobalt nanoparticle catalyst (CoN-BC-0.3) (Figure 7e) using natural bamboo as a carbon source and successfully constructed a structure of helical carbon nanotubes (HCNTs) by mixing bamboo powder with melamine and cobalt chloride and pyrolyzing it under argon atmosphere at 900 °C (Figure 7f,g) [120]. The liquid Zn–air battery based on this catalyst showed excellent performance: an OCV of 1.465 V (Figure 7h,i) and a peak power density of 226 mW cm<sup>-2</sup> (Figure 7j), which highlights the potential of biomass resources for energy storage applications through the synergistic effect of the multi-stage pores of bamboo and helical carbon nanotubes. Along similar lines, our group reported ultrafine pod-like ZnCo/N-CNTs [121]. Using single-celled spirulina as a template, carbon nanotubes with a pod-like structure were obtained (Figure 7k,l). ZnCo/N-CNTs have an average diameter of ~20 nm, and the surface fold interface provides abundant edge active sites where Co coexists in the form of ultrafine nanoparticles (~13.7 nm) and Co-N<sub>x</sub> single atoms. In 1 M KOH electrolyte, ZnCo/N-CNTs exhibited excellent bifunctional catalytic performance: the half-wave potential (0.90 V vs. RHE) (Figure 7m); the OER overpotential was 340 mV. The natural pore structure of biomass combined with transition metal nitrogen-doped carbon-based catalysts can effectively promote oxygen diffusion and ORR, thus effectively reducing the concentration polarization and activation polarization of metal–air batteries.

### 3.4. Metal–H<sub>2</sub>O<sub>2</sub> Batteries

Conventional metal–air batteries rely heavily on the presence of oxygen in the air, fail in low and no-oxygen environments, and face problems such as electrolyte volatilization and the formation of carbonates from CO<sub>2</sub> in the air to clog the electrodes [34,122]. As an oxygen source, hydrogen peroxide (H<sub>2</sub>O<sub>2</sub>) has an ultra-high oxygen content (about 13.5 mol L<sup>-1</sup> in a 70% H<sub>2</sub>O<sub>2</sub> solution), which is 1600 times higher than the concentration of O<sub>2</sub> in air and about three times that of a high-pressure oxygen cylinder (12 MPa) [123,124]. And H<sub>2</sub>O<sub>2</sub> can be conveniently stored in plastic drums, without the need for high-pressure devices. The high-purity oxygen produced by the decomposition of H<sub>2</sub>O<sub>2</sub> can provide an additional driving force for the concentration polarization caused by insufficient oxygen diffusion under high current density and effectively inhibit the corrosion of the air cathode caused by carbonate formation. Consequently, at the structural level, metal–H<sub>2</sub>O<sub>2</sub> batteries indirectly suppress the impact of concentration polarization on traditional metal–air batteries. H<sub>2</sub>O<sub>2</sub> was first applied to an aluminium-hydrogen peroxide (Al-H<sub>2</sub>O<sub>2</sub>) battery in 1969 [124]. Swift Enterprises Ltd. et al. optimized the design and performance of an Al-H<sub>2</sub>O<sub>2</sub> semi-fuel battery through the innovative design of a high-purity Al sheet anode and a gold-plated mesh cathode combined with a flow-through system [125]. Sun and his co-workers developed a Mg-H<sub>2</sub>O<sub>2</sub> battery with a dual-electrolyte that completed 3000 deep-sea tests [126]. Unlike the above mentioned dual-electrolyte Al-H<sub>2</sub>O<sub>2</sub> and Mg-H<sub>2</sub>O<sub>2</sub> structures (Figure 8a,b), our group reported, for the first time, a novel single electrolyte Zn-H<sub>2</sub>O<sub>2</sub> battery based on an H<sub>2</sub>O<sub>2</sub> solution (Figure 8c) and confirmed that it can be successfully used in underwater environments and that its high safety and power can be demonstrated [26,127]. The composition of a Zn-H<sub>2</sub>O<sub>2</sub> battery is as follows: KOH solution as the electrolyte, H<sub>2</sub>O<sub>2</sub> as the oxygen source, activated carbon membrane as the GDL, carbon-based catalyst as the catalyst, and pure Zn as the anode. Unlike Zn-air batteries, Zn-H<sub>2</sub>O<sub>2</sub> batteries have a new sealed compartment to contain H<sub>2</sub>O<sub>2</sub> and the catalyst that decomposes it. The oxygen production from H<sub>2</sub>O<sub>2</sub> decomposition (Equation (12)) is adsorbed and transferred in the GDL, and then ORR occurs on the catalyst layer. The generated OH<sup>-</sup> reacts with metallic zinc on the anode to produce soluble Zn(OH)<sub>4</sub><sup>2-</sup>, then it is converted to insoluble ZnO deposited on the surface of the zinc anode. The total reaction of the discharge process is Equation (13).

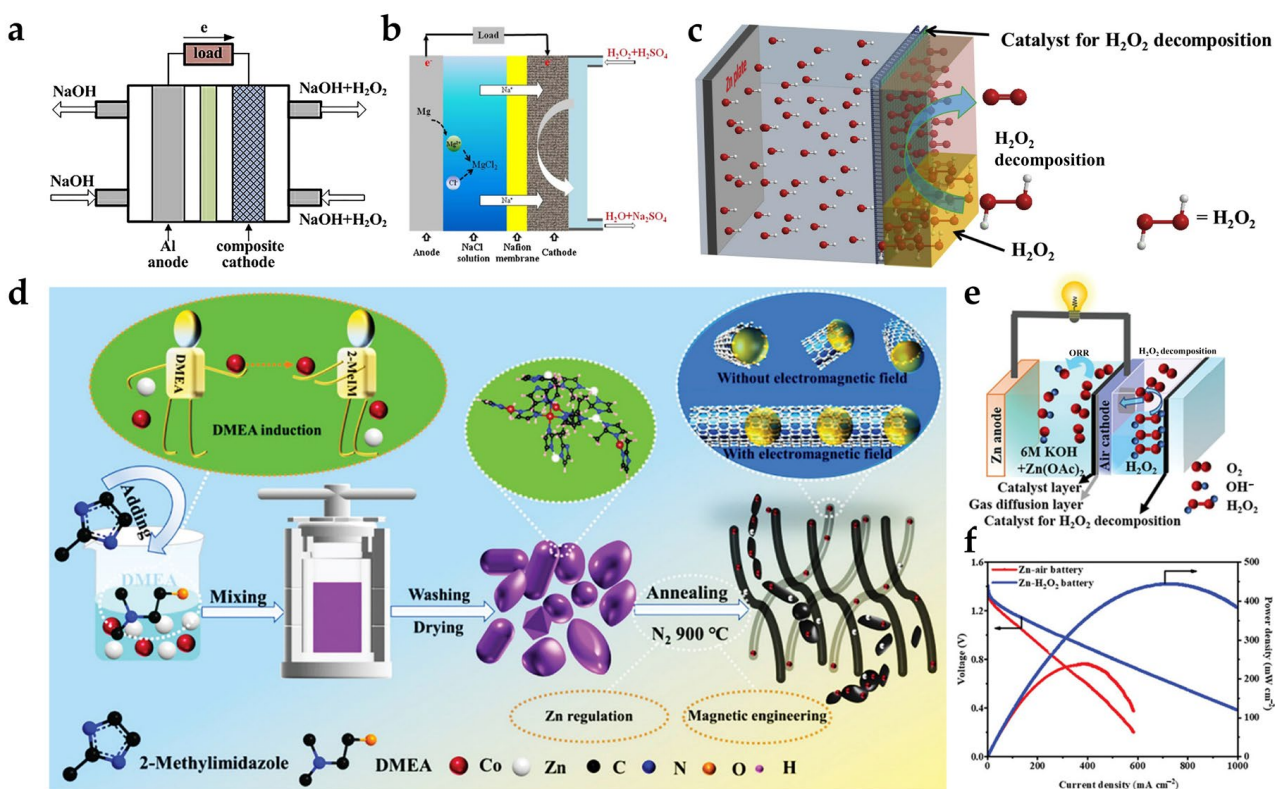
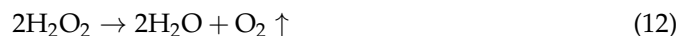


**Figure 8.** (a) Schematic diagram of Al-H<sub>2</sub>O<sub>2</sub> semi-fuel cell configuration (Adapted with permission from Ref. [128], Elsevier 2019.); (b) The schematic structure of a Mg-H<sub>2</sub>O<sub>2</sub> fuel cell (Adapted with permission from Ref. [129], Elsevier 2012.); (c) Schematic illustration of the proposed Zn-H<sub>2</sub>O<sub>2</sub> battery (Adapted with permission from Ref. [127], Elsevier 2020.); (d) Schematic illustration of the synthetic process of ZnCo-NC-DMEA-900; (e) schematic illustration of Zn-H<sub>2</sub>O<sub>2</sub> batteries; (f) discharge polarization curves and the corresponding power density plots (Adapted with permission from Ref. [26], John Wiley and Sons 2022.).

The discharging process:



With the high concentration of oxygen from the decomposition of H<sub>2</sub>O<sub>2</sub> at the air cathode, the ORR and OER performance of the cathode catalyst is challenged. Our group reports an efficient bifunctional electrocatalyst (ZnCo-NC-DMEA-900) with a multi-strategy design for enhancing the power density and stability of underwater Zn-H<sub>2</sub>O<sub>2</sub> batteries [26]. ZnCo-NC-DMEA-900 was synthesized by the strategies of DMEA solvent-induced crystallization, Zn ion activation, and magnetic field-controlled carbon nanotube growth (Figure 8d), exhibiting excellent ORR and OER activities. The peak power density of the Zn-H<sub>2</sub>O<sub>2</sub> battery reached 442 mW cm<sup>-2</sup> (Figure 8e,f), an 85% improvement over comparable Zn-air batteries (238 mW cm<sup>-2</sup>). The energy density is 966 Wh kg<sup>-1</sup> (50 mA cm<sup>-2</sup>) and has been successfully applied to high-power underwater Zn-H<sub>2</sub>O<sub>2</sub> batteries.

## 4. Anode Protection via Electrolyte Engineering

### 4.1. Electrolyte Additives

The electrolyte is a key component of a metal–air battery, providing a channel for charge transfer between the metal anode and the air cathode. The ionic conductivity of the electrolyte directly affects the internal resistance and power output efficiency of the

battery [122]. Traditional aqueous electrolytes face problems such as evaporation [130], carbonation (reaction with CO<sub>2</sub>) [122], and the side reaction of some metals (e.g., Al) with water strongly aggravates their battery polarization [131]; organic electrolytes for Li–air batteries also face problems such as low oxygen solubility, leading to cathodic reaction rate limitation [33]. Zhang et al. effectively solved the carbonization problem of Zn–air batteries by simply introducing a Ca<sup>+</sup> additive, which increased the cycle life of the battery by 22.2% [132]. Wan et al. used a fluorocarbon additive to significantly increase the oxygen solubility in the electrolyte, which resulted in a Li–air battery with a mass power density of 10<sup>4</sup> Wh kg<sup>-1</sup> [133].

In Al–air batteries, the severe self-corrosion of Al anodes in alkaline electrolytes leads directly to low energy efficiency and significant capacity loss. Therefore, effectively inhibiting the corrosion reaction of Al anodes is crucial to improving the performance of Al–air batteries as a whole [134]. Meng et al. investigated the performance of the Al-0.1Sn-0.1In-0.05Ga alloy when used as the anode in Al–air batteries [135]. This alloy contains nanoscale second-phase particles and a uniform microstructure, which effectively inhibits local crystal corrosion. An Al–air battery with an Al-0.1Sn-0.1In-0.05Ga anode exhibits a discharge voltage of 1.523 V, a discharge capacity of 2214 Ah kg<sup>-1</sup>, and an anode efficiency of 74.31%. However, the effect of a single alloyed anode on inhibiting corrosion is minimal. Recent studies show that electrolyte additives form a protective film on the Al anode, effectively inhibiting corrosion. Therefore, investigating these additives is crucial to suppress the Al anode's self-corrosion and enhance battery performance, as summarized in Table 3 [13,136]. Corrosion inhibitors for Al air batteries can be divided into inorganic corrosion inhibitors, organic corrosion inhibitors, and composite corrosion inhibitors. Inorganic corrosion inhibitors (e.g., ZnO) reduce active site corrosion by forming a passivation layer through electrochemical deposition of metal ions on the Al surface [13,137]. Wei et al. investigated the inhibition effect of different Zn<sup>2+</sup> concentrations (0.1–0.5 M) on Al anode self-corrosion by adding ZnO, ZnCO<sub>3</sub>, and ZnCl<sub>2</sub>, respectively, to a 6 M KOH electrolyte (Figure 9a) [138]. SEM showed (Figure 9b) that the Zn layer on the surface of the Al anode in the ZnCl<sub>2</sub> group was dense and smooth, whereas there were cracks in the ZnO group, uneven deposition in the ZnCO<sub>3</sub> group, and the strong Lewis acid groups generated by the ionization of ZnCl<sub>2</sub> adsorbed on the surface of the Al anode, forming a dense and uniform Zn protective layer and significantly reducing the active hydrogen precipitation sites.

Organic corrosion inhibitors reduce the rate of self-corrosion by adsorbing on the Al surface to form a protective film and inhibiting hydrogen precipitation side reactions [136]. Our group proposes an innovative tripodal molecular armoring strategy using cyanuric acid (CA) as an ultrashort-chain corrosion inhibitor to solve the self-corrosion problem of Al anode in Al–air batteries [136], where the planar triacid groups of CA are tightly adsorbed on the Al surface through the Al–O bond (bond length of 2.38 Å) in a “face-to-face” configuration to form a single-molecule protective layer (Figure 9c). It was shown that the addition of 4 M KOH electrolyte with 80 mM CA reduced the Al corrosion rate by 53.5% (to 0.112 mg cm<sup>-2</sup>·min<sup>-1</sup>), and the corrosion potential (E<sub>corr</sub>) of the Al anode was negatively shifted from -1.519 V in the blank group to -1.534 V (Figure 9f). The Al–air battery achieved 2680 mAh g<sup>-1</sup> at a high current density of 50 mA cm<sup>-2</sup> (Figure 9i) and an anode utilization of 89.9%. Compared with the structurally similar BTCA corrosion inhibitor, CA has a denser surface coverage and 52.87% corrosion inhibition efficiency (BTCA only 25.13%) due to its unique tripod configuration (adsorption energy -33.99 kcal mol<sup>-1</sup>) (Figure 9d,e,g,h), and the molecular simulation further reveals that its parallel adsorption structure can effectively shield water/OH<sup>-</sup> erosion. Organic–inorganic hybrid corrosion inhibitors combine the advantages of organic and inorganic corrosion inhibitors and can provide stronger inhibition effects at small doses to further enhance the protection of Al

anodes [13]. Jiang et al. used the three-dimensional porous Al foam as the anode and systematically explored the composite system of ZnO and organic acid (acetic acid, citric acid, EDTA) on the Al self-corrosion [139]. As a phase-forming corrosion inhibitor, ZnO deposits a metallic Zn film on the Al surface to cover the hydrogen precipitation active sites, but the Zn film formed when it is used alone is loose in structure and prone to oxidative flaking. The introduction of organic acids significantly optimized this process, as the carbonyl oxygen atoms in the organic acid molecules bind to the Al surface or the Zn film by chemisorption, forming a stable RCOO-Al and RCOO-Zn composite protective layer. This synergistic effect effectively inhibits the oxidation of the Zn film and enhances the densification and bonding of the film layer, thus significantly reducing the corrosion rate of Al.

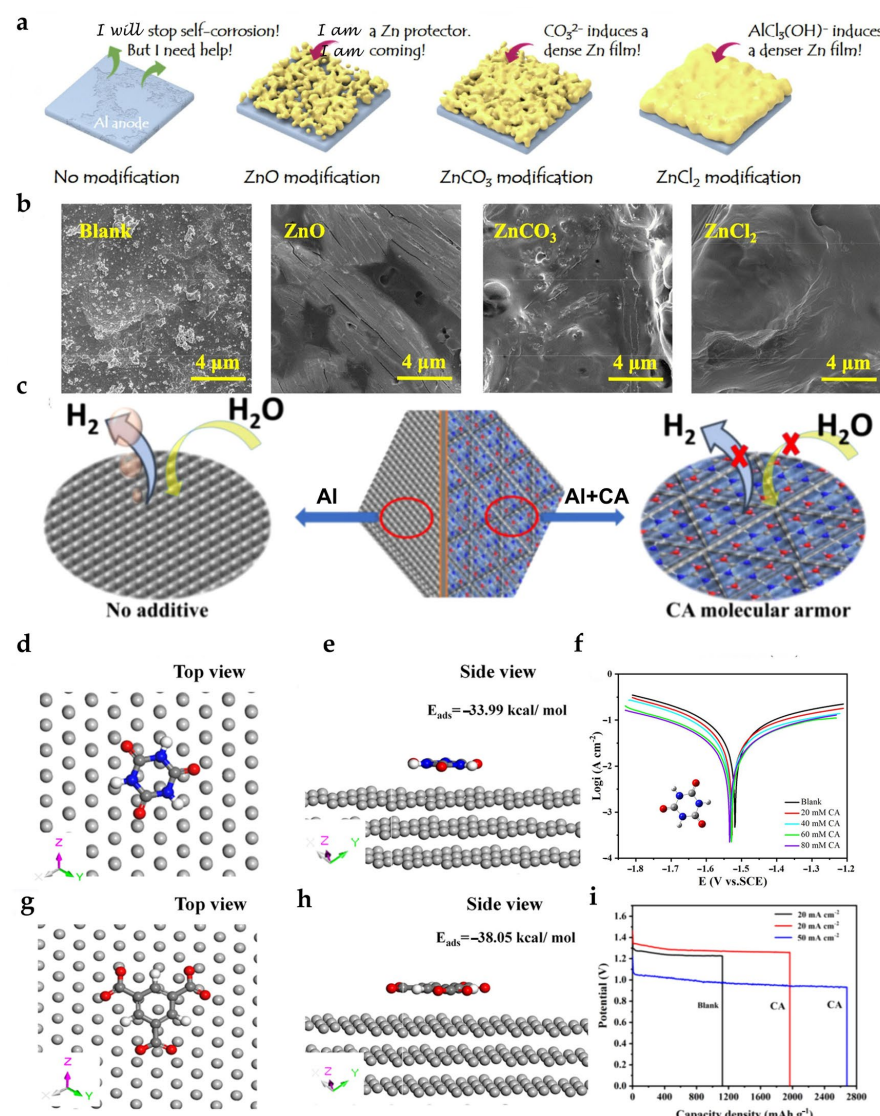


**Figure 9.** (a) Schematic diagram of using inorganic Zn-containing additives to modify the Al anode of AAB; (b) SEM diagrams of AA1060 alloy surface after 60 min immersion in 6 M KOH electrolytes containing blank and 0.5 M various additives (Adapted with permission from Ref. [138], Elsevier 2022.); (c) Proposed corrosion mechanism of the Al anodes with/without the CA in 4 M KOH; (d) top-view and (e) side-view images of CA adsorption on Al (111) surface; (f) tafel polarization curves for Al anode in 4 M KOH with CA.; (g) top-view and (h) side-view images of BTCA adsorption on Al (111) surface; (i) galvanostatic discharge curves of Al anode in the Al-air battery with/without additives at 20 and 50 mA cm<sup>-2</sup> (Adapted with permission from Ref. [136], American Chemical Society 2025.).

**Table 3.** Inhibition of Al corrosion and Al–air battery performance of previously reported electrolyte additives.

Material	Additive	Inhibition Efficiency (%)	Anode Utilization Rate (%)	Capacity Density (m Ah g <sup>-1</sup> )	Current Density (mA cm <sup>-2</sup> )	Ref.
Al alloy 1060	CA	52.87	89.9	2680	50	[136]
Al-5052 alloy	$\beta$ D + DDBAB + 8-HQ	87.2	84.5	2517	20	[131]
Pure Al (99.99%)	Nonoxynol-9	92.8	81.2	2320	20	[140]
Al-5052 alloy	L-tryptophan	67.66	90.76	2702.7	20	[141]
Al alloy	APG + K <sub>2</sub> SnO <sub>3</sub>	94.14	73.87	2180	100	[13]
Al-5052 alloy	8-HQ + DG	83.7	92.3	2748	20	[142]
Al-5052 alloy	8-HQ + ZnO	71.59	70.3	2094	20	[143]
Al-0.5Mg-0.1Sn-0.1Ga alloy	Cerium Acetate + L-Glu	77.85	-	2985.075	20	[144]
Al alloy	NBLT	73.9	82.9	2469.1	20	[145]
Al alloy	AMIB	60	86.1	2564	20	[146]

#### 4.2. Solid-State Electrolytes (SSEs)

Metal–air batteries face problems such as metal dendrite formation [21,55], anode self-corrosion [35,147], electrolyte volatilization [148], and high overpotential during long-term operation [122]. To fundamentally solve the above bottlenecks in safety, lifetime, and efficiency brought about by liquid electrolytes, solid-state electrolytes are regarded as a promising and transformative strategy [149]. Solid-state electrolytes utilize solid-state ionic conductors instead of liquid systems and are characterized by high mechanical strength, good thermal stability, and a wide operating temperature range [29,50,150]. Currently, researchers have applied SSEs to metal–air batteries and have made some progress [119,151–153]. Sun et al. developed a high-performance composite gel electrolyte (PPM) based on PVA, which was successfully applied to a long-life, fully flexible Al–air battery system [151]. For Li–air battery, the low solubility of the discharge products (e.g., Li<sub>2</sub>O<sub>2</sub>) in electrolytes, which tend to be easily deposited on the surface of the electrodes to form passivation layers. SSEs have been shown to inhibit anode passivation caused by lithium dendrites and the shuttle effect of reaction products, thereby providing excellent protection for the anode [49,50]. Cui et al. proposed a polymer-constrained gel electrolyte (PCG) that uses hydrogen bonding to disrupt the low-temperature crystalline structure of DMSO by confining the high donor number solvent DMSO in a BSDE polymer matrix [152]. The electrolyte has an ionic conductivity of 0.15 mS cm<sup>-1</sup> at –20°C (5.5 times that of liquid DMSO), enabling Li–air batteries to be cycled for 450 h at –20°C and 760 h at 25°C, which is significantly better than the liquid electrolyte system. Shang et al. used acrylamide–acrylic acid copolymer (PAMA) as a substrate and introduced AMPNa and Fe<sup>3+</sup>, forming a physical–chemical double cross-linked hydrogel (PAMA-ANa/Fe<sup>3+</sup>) [154]. Strong interfacial adhesion was achieved by utilizing the multiple non-covalent bonds (hydrogen bonding,  $\pi$ - $\pi$  stacking) of AMPNa. Chen et al. used a dynamic hydrogen bonding network (ATAC-EG -PAA) to lock the water and confer self-healing properties [155].

Inspired by the absorption of water from the air by desert plants (e.g., cacti), Zhang et al. designed a novel electrolyte system based on the coordination of Zn(OTF)<sub>2</sub> and acetamide (C<sub>2</sub>H<sub>5</sub>NO) (Figure 10a) [156]. The electrolyte was prepared by one-step UV-initiated radical polymerization to form a dual network structure (WIS-PAA/CNF) with PAA as the main body and cellulose nanofibers (CNFs) as the reinforcement (Figure 10b–d). Its dynamic adsorption–desorption equilibrium enabled the electrolyte to gain about 4% weight instead of losing it after one week at 60% relative humidity (Figure 10g). The introduction of CNF significantly enhanced the tensile strength (22.3 kPa) and ductility (770% elongation at break) of the electrolyte through hydrogen bonding and physical entanglement (Figure 10e). Meanwhile, the free-state –NH<sub>2</sub> group released by coordination gives the electrolyte

excellent adhesion (1.3–2.0 kPa), which enables it to be tightly adhered to Zn anode, carbon cloth, or nickel foam electrode. (Figure 10f). When applied to Zn–air batteries, WIS-PAA/CNF electrolytes exhibit 1300 h of ultra-long cycle stability (Figure 10h) and can drive LED lights, an electronic watch, and a temperature and humidity sensor (Figure 10i).

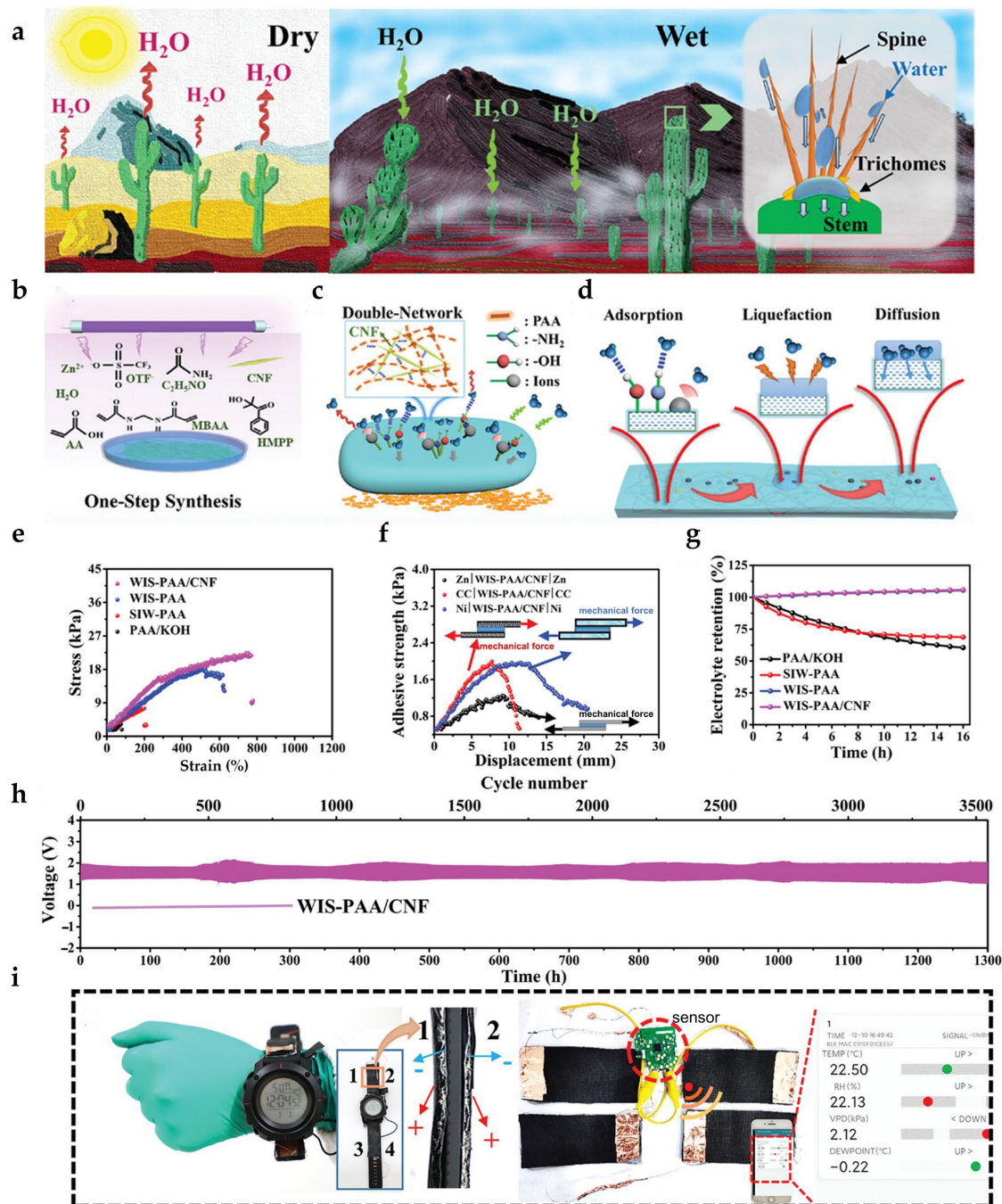


**Figure 10.** Schematic illustrations of (a) cactus absorbing water from ambient air; (b) synthetic method of WIS-PAA/CNF; (c) double-network structure, and (d) water absorption mechanism; (e) adhesive property of WIS-PAA/CNF with Zn, Ni, and CC; (f) tensile stress–strain curves of gel polymer electrolytes; (g) electrolyte retention properties of as-prepared gel polymer electrolytes; (h) long-term cycling performance of ZAB based on WIS-PAA/CNF at 0.1 mA cm<sup>-2</sup> in ambient air with 22 min per cycle (10 min of discharge followed by 10 min of charge and a short interval of 1 min between charge and discharge); (i) the ZABs based on WIS-PAA/CNF in series powered an electronic watch and a temperature and humidity sensor (Adapted with permission from Ref. [156], John Wiley and Sons 2022.).

## 5. Conclusions and Perspectives

In this review, we systematically summarize the main factors contributing to the voltage polarization of metal–air batteries and the corresponding solution strategies, including both the optimal design of air cathodes and electrolyte engineering. In terms of the optimal design of the air cathode, the oxygen reactivity and electrode durability have been significantly enhanced by developing highly efficient, stable, and low-cost bi-functional catalysts (e.g., single-atom catalysts, low-platinum catalysts) and optimizing the electrode structure (e.g., constructing hierarchical porous conductive networks, precisely tuning the three-phase reactive interfaces, and enhancing the stability of the carbon carriers). However, the intrinsic activity, long-term stability, and practical performance of the catalysts in complex reaction environments still need to be further improved; the dynamic evolution and mechanical stability of the electrode structure during deep charging and discharging also need to be more deeply understood and controlled. In electrolyte engineering, to address the volatility, carbonation, and metal anode corrosion/dendritic problems of aqueous electrolytes, as well as the low oxygen solubility, poor electrical conductivity, and poor compatibility with electrode materials (especially anode) of non-aqueous electrolytes, researchers have made positive advances in the areas of improving ionic conductivity, suppressing side reactions, and enhancing interfacial stability and safety through the development of functionalized additives, as well as solid electrolytes and other strategies. In particular, the introduction of solid-state electrolytes provides a fundamental way to solve the problems of volatilization, leakage, and dendrite penetration, but their room-temperature ionic conductivity, solid–solid interfacial contact impedance with the electrodes, and stability are still great challenges. Looking ahead, the development of metal–air batteries needs to be sustained and deepened in the following directions:

1. Combine *in situ* characterization and multi-physics field modeling to reveal the correlation between atomic-scale reaction pathways and macroscopic properties during polarization and guide the rational design of materials. In-depth exploration of novel bifunctional catalysts with atomic-scale active sites, high intrinsic activity, and excellent stability. As shown in Table 1, single atom catalysts have high ORR and OER activities, combined with machine learning to screen the optimal coordination environment, combines the large specific surface area of biomass with the high activity of single atoms and designs bifunctional high-efficiency catalysts with high activity and high oxygen diffusion; precious metals, such as Pt and Ir, are introduced into the catalyst structure in single-atom form, making full use of the active sites of the precious metals to improve the catalytic efficiency. Develop a smarter and more stable electrode structure design to achieve efficient transport and rapid conversion of reactants and products while effectively inhibiting carbon corrosion and structure collapse. Flexible and wearable batteries also place higher demands on the anode structure. Explore the coupling of metal–H<sub>2</sub>O<sub>2</sub> batteries with renewable energy sources (e.g., seawater electrolysis to make H<sub>2</sub>O<sub>2</sub>) to build a closed-loop system.
2. Continue to explore new types of liquid electrolytes (e.g. highly concentrated electrolytes, new solvent systems) with high oxygen solubility/diffusion coefficient, wide electrochemical window, excellent chemical/electrochemical stability, and good interfacial compatibility; design smart additives with “one dose, multiple effects” to synergistically solve the problems of anode protection, oxygen reaction promotion, electrolyte stability, and inhibition of side reactions. Design of intelligent additives to synergistically solve the problems of metal anode protection, oxygen reaction promotion, electrolyte stability, and inhibition of side reactions. Optimize the interfacial compatibility of solid electrolyte and solve the contact impedance problem at the elec-

trode/electrolyte interface; optimize the interfacial compatibility of solid electrolyte and solve the contact impedance problem at the electrode/electrolyte interface.

By continuing to conduct innovative research in the two core areas of air cathode optimization and electrolyte engineering and strengthening the synergistic design and system integration of the two, metal–air batteries are expected to overcome the existing bottlenecks and achieve a wider range of applications in areas such as portable electronic devices, electric vehicles, and large-scale energy storage.

**Author Contributions:** J.L.: Conceptualization, investigation, formal analysis, methodology, project administration, resources, supervision, validation, visualization, writing—original draft, writing—review and editing. B.M.: Investigation, literature review, formal analysis, methodology, visualization, writing—original draft, validation, resources, writing—review and editing. D.H.: Formal analysis, visualization, validation, writing—review and editing. X.W.: project administration, writing—review and editing. All authors have read and agreed to the published version of the manuscript.

**Funding:** This research was funded by the National Natural Science Foundation of China (U1832136), the Natural Science Foundation of Anhui Province (305067828053), and the Fundamental Research Funds for the Central Universities (PA2024GDGP0042 and PA2025GDGP0025).

**Data Availability Statement:** No new data were created or analyzed in this study. Data sharing is not applicable to this article.

**Conflicts of Interest:** The authors declare no conflicts of interest.

## Abbreviations

ORR	Oxygen Reduction Reaction
OER	Oxygen Evolution Reaction
NMC811	$\text{LiNi}_{0.8}\text{Mn}_{0.1}\text{Co}_{0.1}\text{O}_2$
UAV	Unmanned Aerial Vehicle
PVA	Polyvinyl Alcohol
GDL	Gas Diffusion Layer
SAC	Single-Atom Catalyst
DAC	Dual-Atom Catalyst
OCV	Open Circuit Voltage
XAES	X-ray Absorption Fine Structure
XANES	X-ray Absorption Near Edge Structure
EXAFS	Extended X-ray Absorption Fine Structure
HAADF-STEM	High-Angle Annular Dark-Field Scanning Transmission Electron Microscopy
MA	Melamine
DMF	N,N-Dimethylformamide
SEM	Scanning Electron Microscope
TEM	Transmission Electron Microscope
XRD	X-ray Diffraction
XPS	X-ray Photoelectron Spectroscopy
RHE	Reversible Hydrogen Electrode
EDS	Energy Dispersive Spectroscopy
HEA	High Entropy Alloy
DFT	Density Functional Theory
DMEA	N,N-Dimethylethanolamine
CD	Carbon Dot
ZAB	Zn-Air Battery
CNF	Cellulose Nanofiber
PAA	Polyacrylic Acid
CNT	Carbon Nanotube

CA	Cyanuric Acid
BTCA	Benzenetricarboxylic Acid
EDTA	Ethylenediaminetetraacetic Acid
8-HQ	8-Hydroxyquinoline
DDBAB	Dodecyl Dimethyl Benzyl Ammonium Bromide
APG	Alkyl Polyglucoside
$\beta$ D	Dodecyl- $\beta$ -D-Maltoside
DG	Decyl Glucoside
NBLT	$\text{N}\alpha\text{-Boc-N}1\text{-formyl-L-Tryptophan}$
AMIB	1-Aminopropyl-3-Methylimidazolium Bromide
DMSO	Dimethyl Sulfoxide
EG	Ethylene Glycol
ATAC	(3-Acrylamidopropyl) Trimethylammonium Chloride
AMPNa	Sodium Adenosine-5'-Monophosphate
SSE	Solid-State Electrolyte
BSDE	4,4'-Bis(stearoylamino)diphenyl Ether
LED	Light Emitting Diode

## References

- Asenbauer, J.; Eisenmann, T.; Kuenzel, M.; Kazzazi, A.; Chen, Z.; Bresser, D. The success story of graphite as a lithium-ion anode material—Fundamentals, remaining challenges, and recent developments including silicon (oxide) composites. *Sustain. Energy Fuels* **2020**, *4*, 5387–5416. [[CrossRef](#)]
- Kim, U.H.; Jun, D.W.; Park, K.J.; Zhang, Q.; Kaghazchi, P.; Aurbach, D.; Major, D.T.; Goobes, G.; Dixit, M.; Leifer, N.; et al. Pushing the limit of layered transition metal oxide cathodes for high-energy density rechargeable Li ion batteries. *Energy Environ. Sci.* **2018**, *11*, 1271–1279. [[CrossRef](#)]
- McNulty, D.; Carroll, E.; O'Dwyer, C. Rutile TiO<sub>2</sub> Inverse Opal Anodes for Li-Ion Batteries with Long Cycle Life, High-Rate Capability, and High Structural Stability. *Adv. Energy Mater.* **2017**, *7*, 1602291. [[CrossRef](#)]
- Li, W.; Lee, S.; Manthiram, A. High-Nickel NMA: A Cobalt-Free Alternative to NMC and NCA Cathodes for Lithium-Ion Batteries. *Adv. Mater.* **2020**, *32*, 2002718. [[CrossRef](#)] [[PubMed](#)]
- Sabhapathy, P.; Raghunath, P.; Sabbah, A.; Shown, I.; Bayikadi, K.S.; Xie, R.-K.; Krishnamoorthy, V.; Lin, M.-C.; Chen, K.-H.; Chen, L.-C. Axial Chlorine Induced Electron Delocalization in Atomically Dispersed FeN<sub>4</sub> Electrocatalyst for Oxygen Reduction Reaction with Improved Hydrogen Peroxide Tolerance. *Small* **2023**, *19*, 2303598. [[CrossRef](#)]
- Bi, X.; Jiang, Y.; Chen, R.; Du, Y.; Zheng, Y.; Yang, R.; Wang, R.; Wang, J.; Wang, X.; Chen, Z. Rechargeable Zinc–Air versus Lithium–Air Battery: From Fundamental Promises Toward Technological Potentials. *Adv. Energy Mater.* **2024**, *14*, 2302388. [[CrossRef](#)]
- Mori, R. Recent Developments for Aluminum–Air Batteries. *Electrochem. Energy Rev.* **2020**, *3*, 344–369. [[CrossRef](#)]
- Li, Y.; Lu, J. Metal–Air Batteries: Will They Be the Future Electrochemical Energy Storage Device of Choice? *ACS Energy Lett.* **2017**, *2*, 1370–1377. [[CrossRef](#)]
- Pei, P.; Wang, K.; Ma, Z. Technologies for extending zinc–air battery's cyclife: A review. *Appl. Energy* **2014**, *128*, 315–324. [[CrossRef](#)]
- Ma, J.; Quhe, R.; Zhang, W.; Yan, Y.; Tang, H.; Qu, Z.; Cheng, Y.; Schmidt, O.G.; Zhu, M. Zn Microbatteries Explore Ways for Integrations in Intelligent Systems. *Small* **2023**, *19*, e2300230. [[CrossRef](#)] [[PubMed](#)]
- Zhang, H.; Qu, Z.; Tang, H.; Wang, X.; Koehler, R.; Yu, M.; Gerhard, C.; Yin, Y.; Zhu, M.; Zhang, K.; et al. On-Chip Integration of a Covalent Organic Framework-Based Catalyst into a Miniaturized Zn–Air Battery with High Energy Density. *ACS Energy Lett.* **2021**, *6*, 2491–2498. [[CrossRef](#)]
- Zhang, J.; Huang, Y.; Yang, Q.; Venkatesh, V.; Synodis, M.; Pikul, J.H.; Bidstrup Allen, S.A.; Allen, M.G. High-Energy-Density Zinc–Air Microbatteries with Lean PVA–KOH–K<sub>2</sub>CO<sub>3</sub> Gel Electrolytes. *ACS Appl. Mater. Interfaces* **2023**, *15*, 6807–6816. [[CrossRef](#)]
- Wu, S.; Zhang, Q.; Sun, D.; Luan, J.; Shi, H.; Hu, S.; Tang, Y.; Wang, H. Understanding the synergistic effect of alkyl polyglucoside and potassium stannate as advanced hybrid corrosion inhibitor for alkaline aluminum-air battery. *Chem. Eng. J.* **2020**, *383*, 123162. [[CrossRef](#)]
- Lv, C.; Zhu, Y.; Li, Y.; Zhang, Y.; Kuang, J.; Tang, Y.; Li, H.; Wang, H. Hydrogen-bonds reconstructing electrolyte enabling low-temperature aluminum-air batteries. *Energy Storage Mater.* **2023**, *59*, 102756. [[CrossRef](#)]
- Kondori, A.; Esmaeilirad, M.; Harzandi, A.M.; Amine, R.; Saray, M.T.; Yu, L.; Liu, T.; Wen, J.; Shan, N.; Wang, H.-H.; et al. A room temperature rechargeable Li<sub>2</sub>O-based lithium-air battery enabled by a solid electrolyte. *Science* **2023**, *379*, 499–505. [[CrossRef](#)]

16. Nazir, G.; Rehman, A.; Lee, J.-H.; Kim, C.-H.; Gautam, J.; Heo, K.; Hussain, S.; Ikram, M.; AlObaid, A.A.; Lee, S.-Y.; et al. A Review of Rechargeable Zinc–Air Batteries: Recent Progress and Future Perspectives. *Nano-Micro Lett.* **2024**, *16*, 138. [CrossRef] [PubMed]
17. Bruce, P.G.; Freunberger, S.A.; Hardwick, L.J.; Tarascon, J.-M. Li–O<sub>2</sub> and Li–S batteries with high energy storage. *Nat. Mater.* **2012**, *11*, 19–29. [CrossRef]
18. Liu, J.-N.; Zhao, C.-X.; Wang, J.; Ren, D.; Li, B.-Q.; Zhang, Q. A brief history of zinc–air batteries: 140 years of epic adventures. *Energy Environ. Sci.* **2022**, *15*, 4542–4553. [CrossRef]
19. Shao, W.; Yan, R.; Zhou, M.; Ma, L.; Roth, C.; Ma, T.; Cao, S.; Cheng, C.; Yin, B.; Li, S. Carbon-Based Electrodes for Advanced Zinc–Air Batteries: Oxygen-Catalytic Site Regulation and Nanostructure Design. *Electrochem. Energy Rev.* **2023**, *6*, 11. [CrossRef]
20. Wang, H.; Wang, K.; Zuo, Y.; Wei, M.; Pei, P.; Zhang, P.; Chen, Z.; Shang, N. Magnetoelectric Coupling for Metal–Air Batteries. *Adv. Funct. Mater.* **2022**, *33*, 2210127. [CrossRef]
21. Zhu, Y.; Zheng, D.; Xing, X.; Wu, S.; Guo, X.; Liu, J.; Guo, X.; Zhou, J.; Jiao, Y.; Zeng, B.; et al. Advancements in Gel Electrolytes for High-Performance Zinc–Air Batteries to Stabilize Zinc Anodes. *J. Phys. Chem. C* **2024**, *128*, 7007–7025. [CrossRef]
22. Aurbach, D.; McCloskey, B.D.; Nazar, L.F.; Bruce, P.G. Advances in understanding mechanisms underpinning lithium–air batteries. *Nat. Energy* **2016**, *1*, 16128. [CrossRef]
23. Yang, T.; Ge, B.; Liu, X.; Zhang, Z.; Chen, Y.; Liu, Y. Boosting the electrocatalytic activity of single atom iron catalysts through sulfur-doping engineering for liquid and flexible rechargeable Zn–air batteries. *J. Mater. Chem. A* **2024**, *12*, 11669–11680. [CrossRef]
24. Li, B.; Liu, J.; Zhao, C.; Hu, A.; Sun, X.; Mei, B.; Long, J. Carbothermal Reduction-Assisted Synthesis of a Carbon-Supported Highly Dispersed PtSn Nanoalloy for the Oxygen Reduction Reaction. *Inorg. Chem.* **2024**, *63*, 19322–19331. [CrossRef] [PubMed]
25. Zhu, Z.; Jin, L.; Zhou, M.; Fu, K.; Meng, F.; Wei, X.; Liu, J. Single-cell-array biomass-templated architecture of hierarchical porous electrocatalysts for Zn–air and Zn–H<sub>2</sub>O<sub>2</sub> batteries. *Chem. Commun.* **2023**, *59*, 4356–4359. [CrossRef]
26. Yue, C.; Zhang, N.; Zhu, Z.; Chen, P.; Meng, F.; Liu, X.; Wei, X.; Liu, J. Multi-Strategy Architecture of High-Efficiency Electrocatalysts for Underwater Zn–H<sub>2</sub>O<sub>2</sub> Batteries with Superior Power Density of 442 mW cm<sup>-2</sup>. *Small* **2022**, *18*, 2106532. [CrossRef] [PubMed]
27. Miao, D.; Li, S.; Jin, D.; Long, J.; Qu, J.; Wang, Y.; Wu, Z. Hybrid Organic–Inorganic Additive for Robust Al Anode in Alkaline Aluminum–Air Battery. *Small Methods* **2024**, *8*, 2301255. [CrossRef]
28. Jiao, M.; Dai, L.; Ren, H.-R.; Zhang, M.; Xiao, X.; Wang, B.; Yang, J.; Liu, B.; Zhou, G.; Cheng, H.-M. A Polarized Gel Electrolyte for Wide-Temperature Flexible Zinc–Air Batteries. *Angew. Chem. Int. Ed.* **2023**, *62*, e202301114. [CrossRef]
29. Jiang, L.; Luo, X.; Wang, D.-W. A review on system and materials for aqueous flexible metal–air batteries. *Carbon Energy* **2023**, *5*, e284. [CrossRef]
30. Lee, H.; Lee, D.J.; Kim, M.; Kim, H.; Kwon, H.J.; Lee, H.C.; Im, D. High Energy Density Li–Air Battery with the Polymer Electrolyte Coated CNTs Electrode Via Layer-By-Layer Method. *ECS Meet. Abstr.* **2020**, *MA2019-01*, 344. [CrossRef]
31. Zhang, X.; Tsay, K.; Qu, W.; Fahlman, J. Bifunctional air electrode fabrication, performance and stability evaluation. *J. Energy Storage* **2018**, *20*, 520–528. [CrossRef]
32. Chen, J.; Qiu, C.; Zhang, L.; Wang, B.; Zhao, P.; Zhao, Y.; Wang, H.; Yang, G.; Sun, A.; Fan, J.; et al. Wood-derived Fe cluster-reinforced asymmetric single-atom catalysts and weather-resistant organohydrogel for wide-temperature flexible Zn–air batteries. *Energy Environ. Sci.* **2024**, *17*, 4746–4757. [CrossRef]
33. Lai, J.; Xing, Y.; Chen, N.; Li, L.; Wu, F.; Chen, R. Electrolytes for Rechargeable Lithium–Air Batteries. *Angew. Chem. Int. Ed.* **2020**, *59*, 2974–2997. [CrossRef]
34. Chen, Y.; Xu, J.; He, P.; Qiao, Y.; Guo, S.; Yang, H.; Zhou, H. Metal-air batteries: Progress and perspective. *Sci. Bull.* **2022**, *67*, 2449–2486. [CrossRef]
35. Huang, R.-B.; Wang, M.-Y.; Xiong, J.-F.; Zhang, H.; Tian, J.-H.; Li, J.-F. Anode optimization strategies for zinc–air batteries. *eScience* **2025**, *5*, 100309. [CrossRef]
36. Zhang, J.; Chen, A.; Han, S.; Wu, Q.; Chen, Y.; Huang, J.; Guan, L. Self-Powered Integrated System with a Flexible Strain Sensor and a Zinc–Air Battery. *ACS Appl. Mater. Interfaces* **2023**, *15*, 45260–45269. [CrossRef]
37. Wang, Y.; Pan, W.; Kwok, H.Y.H.; Zhang, H.; Lu, X.; Leung, D.Y.C. Liquid-free Al-air batteries with paper-based gel electrolyte: A green energy technology for portable electronics. *J. Power Sources* **2019**, *437*, 226896. [CrossRef]
38. Ma, Z.; Yuan, X.; Li, L.; Ma, Z.-F.; Wilkinson, D.P.; Zhang, L.; Zhang, J. A review of cathode materials and structures for rechargeable lithium–air batteries. *Energy Environ. Sci.* **2015**, *8*, 2144–2198. [CrossRef]
39. Shao, Y.; Ding, F.; Xiao, J.; Zhang, J.; Xu, W.; Park, S.; Zhang, J.-G.; Wang, Y.; Liu, J. Making Li–Air Batteries Rechargeable: Material Challenges. *Adv. Funct. Mater.* **2013**, *23*, 987–1004. [CrossRef]
40. Tan, P.; Chen, B.; Xu, H.; Zhang, H.; Cai, W.; Ni, M.; Liu, M.; Shao, Z. Flexible Zn– and Li–air batteries: Recent advances, challenges, and future perspectives. *Energy Environ. Sci.* **2017**, *10*, 2056–2080. [CrossRef]
41. Wang, L.; Wang, Y.; Qiao, Y.; Wu, S.; Lu, X.; Zhu, J.-J.; Zhang, J.-R.; Zhou, H. Superior efficient rechargeable lithium–air batteries using a bifunctional biological enzyme catalyst. *Energy Environ. Sci.* **2020**, *13*, 144–151. [CrossRef]

42. Shi, Y.; Guo, Z.; Wang, C.; Gao, M.; Lin, X.; Duan, H.; Wang, Y.; Sun, X. Design of multifunctional interfaces on ceramic solid electrolytes for high-performance lithium-air batteries. *Green Energy Environ.* **2025**, *10*, 183–192. [[CrossRef](#)]
43. Jiao, D.; Ma, Z.; Li, J.; Han, Y.; Mao, J.; Ling, T.; Qiao, S. Test factors affecting the performance of zinc-air battery. *J. Energy Chem.* **2020**, *44*, 1–7. [[CrossRef](#)]
44. Iqbal, A.; El-Kadri, O.M.; Hamdan, N.M. Insights into rechargeable Zn-air batteries for future advancements in energy storing technology. *J. Energy Storage* **2023**, *62*, 106926. [[CrossRef](#)]
45. Liu, B.; Dai, Y.-K.; Li, L.; Zhang, H.-D.; Zhao, L.; Kong, F.-R.; Sui, X.-L.; Wang, Z.-B. Effect of polytetrafluoroethylene (PTFE) in current collecting layer on the performance of zinc-air battery. *Prog. Nat. Sci. Mater. Int.* **2020**, *30*, 861–867. [[CrossRef](#)]
46. Zhang, X.; Wu, X.; Lv, Y.; Guo, J.; Liang, N.; Guo, R.; Zhu, Y.; Liu, H.; Jia, D. Fabrication of Zn–Air Battery with High Output Capacity Under Ultra-Large Current. *Small* **2024**, *20*, 2307999. [[CrossRef](#)] [[PubMed](#)]
47. Li, J.; Yan, F.; Su, Z.; Zhang, T.; Zhang, X.; Sun, H. Highly Efficient Li–Air Battery Using Linear Porosity Air Electrodes. *J. Electrochem. Soc.* **2020**, *167*, 090529. [[CrossRef](#)]
48. He, P.; Zhang, T.; Jiang, J.; Zhou, H. Lithium–Air Batteries with Hybrid Electrolytes. *J. Phys. Chem. Lett.* **2016**, *7*, 1267–1280. [[CrossRef](#)] [[PubMed](#)]
49. Pan, K.; Li, M.; Wang, W.; Xing, S.; Dou, Y.; Gao, S.; Zhang, Z.; Zhou, Z. A leap by the rise of solid-state electrolytes for Li-air batteries. *Green Energy Environ.* **2023**, *8*, 939–944. [[CrossRef](#)]
50. Salado, M.; Lizundia, E. Advances, challenges, and environmental impacts in metal–air battery electrolytes. *Mater. Today Energy* **2022**, *28*, 101064. [[CrossRef](#)]
51. Wang, X.; Wen, K.; Song, Y.; Ye, L.; Zhang, K.H.L.; Pan, Y.; Lv, W.; Liao, Y.; He, W. Gas transport evaluation in lithium–air batteries with micro/nano-structured cathodes. *J. Power Sources* **2015**, *274*, 764–767. [[CrossRef](#)]
52. Ye, L.; Lv, W.; Zhang, K.H.L.; Wang, X.; Yan, P.; Dickerson, J.H.; He, W. A new insight into the oxygen diffusion in porous cathodes of lithium-air batteries. *Energy* **2015**, *83*, 669–673. [[CrossRef](#)]
53. Xiong, Q.; Huang, G.; Yu, Y.; Li, C.L.; Li, J.C.; Yan, J.M.; Zhang, X.B. Soluble and Perfluorinated Polyelectrolyte for Safe and High-Performance Li–O<sub>2</sub> Batteries. *Angew. Chem.* **2022**, *61*, e202116635. [[CrossRef](#)]
54. Yu, W.; Shang, W.; Xiao, X.; Ma, Y.; Chen, Z.; Chen, B.; Xu, H.; Ni, M.; Tan, P. Elucidating the mechanism of discharge performance improvement in zinc-air flow batteries: A combination of experimental and modeling investigations. *J. Energy Storage* **2021**, *40*, 102779. [[CrossRef](#)]
55. Ji, H.; Wang, M.; Liu, S.; Sun, H.; Liu, J.; Hou, Z.; Qian, T.; Yan, C. Identifying the Lewis Base Chemistry in Preventing the Deposition of Metal Oxides on Ketone-Enriched Carbon Cathodes for Highly Durable Metal-Air Batteries. *ACS Appl. Mater. Interfaces* **2020**, *12*, 3603–3609. [[CrossRef](#)] [[PubMed](#)]
56. Ran, J.; Chen, P.; Quan, X.; Si, M.; Gao, D. Improving the Oxygen Evolution Reaction Kinetics in Zn-Air Battery by Iodide Oxidation Reaction. *Small* **2024**, *20*, 2402052. [[CrossRef](#)]
57. Balamurugan, J.; Austeria, P.M.; Kim, J.B.; Jeong, E.-S.; Huang, H.-H.; Kim, D.H.; Koratkar, N.; Kim, S.O. Electrocatalysts for Zinc–Air Batteries Featuring Single Molybdenum Atoms in a Nitrogen-Doped Carbon Framework. *Adv. Mater.* **2023**, *35*, 2302625. [[CrossRef](#)]
58. Li, L.; Zhu, Q.Y.; Han, M.J.; Tu, X.B.; Shen, Y. MOF-derived single-atom catalysts for oxygen electrocatalysis in metal-air batteries. *Nanoscale* **2023**, *15*, 13487–13497. [[CrossRef](#)]
59. Fang, C.-Y.; Zhang, X.-H.; Zhang, Q.; Liu, D.; Cui, X.-M.; Xu, J.-C.; Shi, C.-L.; Yang, M.-Y. Single transition-metal atoms anchored on a novel Dirac-dispersive π–π conjugated holey graphitic carbon nitride substrate: Computational screening toward efficient bifunctional OER/ORR electrocatalysts. *Rare Met.* **2024**, *43*, 3819–3832. [[CrossRef](#)]
60. Wang, Q.; Lyu, L.; Hu, X.; Fan, W.; Shang, C.; Huang, Q.; Li, Z.; Zhou, Z.; Kang, Y.-M. Tailoring the Surface Curvature of the Supporting Carbon to Tune the d-Band Center of Fe–N–C Single-Atom Catalysts for Zinc-Urea-Air Batteries. *Angew. Chem. Int. Ed.* **2025**, *64*, e202422920. [[CrossRef](#)]
61. Qiao, B.; Wang, A.; Yang, X.; Allard, L.F.; Jiang, Z.; Cui, Y.; Liu, J.; Li, J.; Zhang, T. Single-atom catalysis of CO oxidation using Pt<sub>1</sub>/FeO<sub>x</sub>. *Nat. Chem.* **2011**, *3*, 634–641. [[CrossRef](#)]
62. Yuan, K.; Lützenkirchen-Hecht, D.; Li, L.; Shuai, L.; Li, Y.; Cao, R.; Qiu, M.; Zhuang, X.; Leung, M.K.H.; Chen, Y.; et al. Boosting Oxygen Reduction of Single Iron Active Sites via Geometric and Electronic Engineering: Nitrogen and Phosphorus Dual Coordination. *J. Am. Chem. Soc.* **2020**, *142*, 2404–2412. [[CrossRef](#)]
63. Han, J.; Meng, X.; Lu, L.; Bian, J.; Li, Z.; Sun, C. Single-Atom Fe-N-C as an Efficient Electrocatalyst for Zinc–Air Batteries. *Adv. Funct. Mater.* **2019**, *29*, 1808872. [[CrossRef](#)]
64. Jang, I.; Lee, S.; Kim, D.-g.; Paidi, V.K.; Lee, S.; Kim, N.D.; Jung, J.Y.; Lee, K.-S.; Lim, H.-K.; Kim, P.; et al. Instantaneous Thermal Energy for Swift Synthesis of Single-Atom Catalysts for Unparalleled Performance in Metal–Air Batteries and Fuel Cells. *Adv. Mater.* **2024**, *36*, 2403273. [[CrossRef](#)]

65. Cao, Y.; Peng, H.; Chu, S.; Tang, Y.; Huang, C.; Wang, Z.; Liu, F.; Wu, J.; Shan, B.; Chen, R. Molten-salt-assisted thermal emitting method to transform bulk  $\text{Fe}_2\text{O}_3$  into Fe single atom catalysts for oxygen reduction reaction in Zn-air battery. *Chem. Eng. J.* **2021**, *420*, 129713. [[CrossRef](#)]
66. Sun, H.; Li, L.; Zhu, Z.; Li, X.; Zhu, Z.; Yuan, T.; Yang, J.; Pang, Y.; Zheng, S. Vacancy-defective nano-carbon matrix enables highly efficient Fe single atom catalyst for aqueous and flexible Zn-Air batteries. *Chem. Eng. J.* **2024**, *496*, 153669. [[CrossRef](#)]
67. Yang, L.; Du, C.; Tian, J.; Yao, X.; Zhang, Q.; Ma, X.; Zhu, Y.; Zou, M.; Cao, C. Fully exposed copper single-atom sites on mesoporous N/S-codoped graphene for efficient zinc-air battery. *Appl. Catal. B Environ. Energy* **2024**, *355*, 124190. [[CrossRef](#)]
68. Li, C.; Zhang, Y.; Yuan, M.; Liu, Y.; Lan, H.; Li, Z.; Liu, K.; Wang, L. A pH-universal ORR catalyst with S heteroatom doping single-atom iron sites derived from a 2D flake-like MOF for superior flexible quasi-solid-state rechargeable Zn-air battery. *Chem. Eng. J.* **2023**, *471*, 144515. [[CrossRef](#)]
69. Yuan, M.; Liu, Y.; Du, Y.; Xiao, Z.; Li, H.; Liu, K.; Wang, L. Dual-Shelled Hollow Leafy Carbon Support with Atomically Dispersed (N,S)-Bridged Hydroxy-Coordinated Asymmetric Fe Sites for Oxygen Reduction. *Adv. Funct. Mater.* **2024**, *34*, 2401484. [[CrossRef](#)]
70. Zhang, S.; Sun, B.; Liao, K.; Wang, X.; Chen, Z.; Wang, J.; Hu, W.; Han, X. Boosting Oxygen Reduction Reaction Performance of Fe Single-Atom Catalysts Via Precise Control of the Coordination Environment. *Adv. Funct. Mater.* **2025**, *35*, 2425640. [[CrossRef](#)]
71. Ji, S.; Mou, Y.; Liu, H.; Lu, X.; Zhang, Y.; Guo, C.; Sun, K.; Liu, D.; Horton, J.H.; Wang, C.; et al. Manipulating the Electronic Properties of an Fe Single Atom Catalyst via Secondary Coordination Sphere Engineering to Provide Enhanced Oxygen Electrocatalytic Activity in Zinc-Air Batteries. *Adv. Mater.* **2024**, *36*, 2410121. [[CrossRef](#)]
72. Xu, C.; Guo, C.; Liu, J.; Hu, B.; Dai, J.; Wang, M.; Jin, R.; Luo, Z.; Li, H.; Chen, C. Accelerating the oxygen adsorption kinetics to regulate the oxygen reduction catalysis via  $\text{Fe}_3\text{C}$  nanoparticles coupled with single  $\text{Fe}-\text{N}_4$  sites. *Energy Storage Mater.* **2022**, *51*, 149–158. [[CrossRef](#)]
73. Sun, S.; Yang, F.; Zhang, X.; Qian, J.; Wei, K.; An, J.; Sun, Y.; Wang, S.; Li, X.; Li, Y. Highly dispersed carbon-encapsulated  $\text{FeS}/\text{Fe}_3\text{C}$  nanoparticles distributed in Fe-N-C for enhanced oxygen electrocatalysis and Zn-air batteries. *Chem. Eng. J.* **2024**, *487*, 150673. [[CrossRef](#)]
74. Srinivas, K.; Chen, Z.; Chen, A.; Ma, F.; Zhu, M.-q.; Chen, Y.  $\text{Fe}-\text{N}_x$  sites coupled with core-shell  $\text{FeS}@\text{C}$  nanoparticles to boost the oxygen catalysis for rechargeable Zn-air batteries. *J. Energy Chem.* **2024**, *90*, 565–577. [[CrossRef](#)]
75. Gu, T.; Zhang, D.; Yang, Y.; Peng, C.; Xue, D.; Zhi, C.; Zhu, M.; Liu, J. Dual-Sites Coordination Engineering of Single Atom Catalysts for Full-Temperature Adaptive Flexible Ultralong-Life Solid-State Zn–Air Batteries. *Adv. Funct. Mater.* **2022**, *33*, 2212299. [[CrossRef](#)]
76. Liu, H.; Jiang, L.; Liu, Y.; Lu, B.; Li, L.; Tang, Y.; Sun, Y.; Zhou, J. Construction of single-atomic Fe and Cu sites within nitrogen/sulfur co-doped carbon matrix for boosting the performance of zinc-air batteries. *Appl. Catal. B Environ. Energy* **2025**, *362*, 124705. [[CrossRef](#)]
77. Cui, T.; Wang, Y.-P.; Ye, T.; Wu, J.; Chen, Z.; Li, J.; Lei, Y.; Wang, D.; Li, Y. Engineering Dual Single-Atom Sites on 2D Ultrathin N-doped Carbon Nanosheets Attaining Ultra-Low-Temperature Zinc-Air Battery. *Angew. Chem. Int. Ed.* **2022**, *61*, e202115219. [[CrossRef](#)]
78. Wang, B.; Tang, J.; Zhang, X.; Hong, M.; Yang, H.; Guo, X.; Xue, S.; Du, C.; Liu, Z.; Chen, J. Nitrogen doped porous carbon polyhedral supported Fe and Ni dual-metal single-atomic catalysts: Template-free and metal ligand-free sysnthesis with microwave-assistance and d-band center modulating for boosted ORR catalysis in zinc-air batteries. *Chem. Eng. J.* **2022**, *437*, 135295. [[CrossRef](#)]
79. Zhao, Z.-H.; Ma, D.; Zhuang, Z.; Wang, K.; Xu, C.; Sun, K.; Deng, S.-Q.; Yan, W.; Zhang, J. Atomically dispersed iron–zinc dual-metal sites to boost catalytic oxygen reduction activities for efficient zinc–air batteries. *Nanoscale* **2025**, *17*, 9515–9524. [[CrossRef](#)]
80. Li, R.; Fan, W.; Rao, P.; Luo, J.; Li, J.; Deng, P.; Wu, D.; Huang, W.; Jia, C.; Liu, Z.; et al. Multimetallic Single-Atom Catalysts for Bifunctional Oxygen Electrocatalysis. *ACS Nano* **2023**, *17*, 18128–18138. [[CrossRef](#)]
81. Yang, J.; Wu, Y.P.; Shi, J.; Liu, H.M.; Liu, Z.Q.; You, Q.W.; Li, X.X.; Cong, L.C.; Liu, D.B.; Liu, F.B.; et al. Effect of Carbon Support on the Properties of Fe, N, S Co-Doped ORR Catalysts Prepared by Molten Salt Method. *J. Electrochem. Soc.* **2024**, *171*, 76507. [[CrossRef](#)]
82. Fei, H.; Dong, J.; Wan, C.; Zhao, Z.; Xu, X.; Lin, Z.; Wang, Y.; Liu, H.; Zang, K.; Luo, J.; et al. Microwave-Assisted Rapid Synthesis of Graphene-Supported Single Atomic Metals. *Adv. Mater.* **2018**, *30*, 1802146. [[CrossRef](#)]
83. Gong, H.; Wei, Z.; Gong, Z.; Liu, J.; Ye, G.; Yan, M.; Dong, J.; Allen, C.; Liu, J.; Huang, K.; et al. Low-Coordinated Co-N-C on Oxygenated Graphene for Efficient Electrocatalytic  $\text{H}_2\text{O}_2$  Production. *Adv. Funct. Mater.* **2022**, *32*, 2106886. [[CrossRef](#)]
84. Sun, J.-K.; Pan, Y.-W.; Xu, M.-Q.; Sun, L.; Zhang, S.; Deng, W.-Q.; Zhai, D. Heteroatom doping regulates the catalytic performance of single-atom catalyst supported on graphene for ORR. *Nano Res.* **2024**, *17*, 1086–1093. [[CrossRef](#)]
85. Zha, S.; Wang, D.; Liu, C.; Wang, W.; Mitsuzaki, N.; Chen, Z. Heteroatom doped M-N-C single-atom catalysts for high-efficiency oxygen reduction reaction: Regulation of coordination configurations. *Sustain. Energy Fuels* **2023**, *943*, 117506. [[CrossRef](#)]
86. Yang, K.-Z.; Xu, C.; Guo, P.-P.; Zhao, Y.-M.; Chi, H.-M.; Xu, Y.; Wei, P.-J.; Zheng, T.; He, Q.; Ren, Q.; et al. Regulating the Electronic Configuration of Single-Atom Catalysts with  $\text{Fe}-\text{N}_5$  Sites via Environmental Sulfur Atom Doping for an Enhanced Oxygen Reduction Reaction. *ACS Sustain. Chem. Eng.* **2024**, *12*, 11033–11043. [[CrossRef](#)]

87. Zhu, S.; Wu, T.; Liao, M.; Meng, J.; Xie, Y.; Lu, C. Regulating the coordination environment of atomically dispersed Fe-N<sub>4</sub> moieties in carbon enables efficient oxygen reduction for Zn-air batteries. *Chem. Eng. J.* **2024**, *484*, 149693. [CrossRef]
88. Xu, C.; Wu, J.; Chen, L.; Gong, Y.; Mao, B.; Zhang, J.; Deng, J.; Mao, M.; Shi, Y.; Hou, Z.; et al. Boric Acid-Assisted Pyrolysis for High-Loading Single-Atom Catalysts to Boost Oxygen Reduction Reaction in Zn-Air Batteries. *ENERGY Environ. Mater.* **2024**, *7*, e12569. [CrossRef]
89. Hu, L.; Dai, C.; Chen, L.; Zhu, Y.; Hao, Y.; Zhang, Q.; Gu, L.; Feng, X.; Yuan, S.; Wang, L.; et al. Metal-Triazolate-Framework-Derived FeN<sub>4</sub>Cl<sub>1</sub> Single-Atom Catalysts with Hierarchical Porosity for the Oxygen Reduction Reaction. *Angew. Chem. Int. Ed.* **2021**, *60*, 27324–27329. [CrossRef]
90. Chen, Y.; He, T.; Liu, Q.; Hu, Y.; Gu, H.; Deng, L.; Liu, H.; Liu, Y.; Liu, Y.-N.; Zhang, Y.; et al. Highly durable iron single-atom catalysts for low-temperature zinc-air batteries by electronic regulation of adjacent iron nanoclusters. *Appl. Catal. B Environ.* **2023**, *323*, 122163. [CrossRef]
91. Yang, Y.; Xiao, Y.; Zhang, L.; Wang, H.-T.; Chen, K.-H.; Lin, W.-X.; Jin, N.; Sun, C.; Shao, Y.-C.; Chen, J.-L.; et al. Encaging Co nanoparticle in atomic CoN<sub>4</sub>-dispersed graphite nanopocket evokes high oxygen reduction activity for flexible Zn-air battery. *Appl. Catal. B Environ. Energy* **2024**, *347*, 123792. [CrossRef]
92. Liu, X.-Y.; Liu, J.-W.; Li, G.; Zhao, J.-X. Transition metal clusters with precise numbers of atoms anchored on graphdiyne as multifunctional electrocatalysts for OER/ORR/HER: A computational study. *Rare Met.* **2024**, *43*, 3107–3117. [CrossRef]
93. Ma, Y.; Fan, H.; Wu, C.; Zhang, M.; Yu, J.; Song, L.; Li, K.; He, J. An efficient dual-metal single-atom catalyst for bifunctional catalysis in zinc-air batteries. *Carbon* **2021**, *185*, 526–535. [CrossRef]
94. Li, Z.; Zhong, X.; Gao, L.; Hu, J.; Peng, W.; Wang, X.; Zhou, G.; Xu, B. Asymmetric Coordination of Bimetallic Fe–Co Single-Atom Pairs toward Enhanced Bifunctional Activity for Rechargeable Zinc–Air Batteries. *ACS Nano* **2024**, *18*, 13006–13018. [CrossRef]
95. Zhou, Y.; Liu, Y.; Wang, Z.; Li, C.; Wang, Z.; Zhang, S.; Deng, C. Fe-Co dual atomic doublets on N, P codoped carbon as active sites in the framework of heterostructured hollow fibers towards high-performance flexible Zn-Air battery. *Energy Storage Mater.* **2023**, *59*, 102772. [CrossRef]
96. Guo, Q.; Yuan, R.; Zhao, Y.; Yu, Y.; Fu, J.; Cao, L. Performance of Nitrogen-Doped Carbon Nanoparticles Carrying FeNiCu as Bifunctional Electrocatalyst for Rechargeable Zinc-Air Battery. *Small* **2024**, *20*, 2400830. [CrossRef] [PubMed]
97. Liu, Q.; Zhang, C.; Ren, M.; Wang, J.; Feng, L.; Wang, Y.; Liu, C.; Xiao, N.; Zhang, H. Sulfur doping triggers charge redistribution at the heterointerface of Fe-N-C supported ultralow-Pt-loading electrocatalysts for efficient oxygen reduction. *Colloids Surf. A Physicochem. Eng. Asp.* **2024**, *692*, 134055. [CrossRef]
98. Pradhan, A.K.; Halder, S.; Chakraborty, C. “Less is more”: Carbon nanostructure-tailored low platinum containing electrocatalysts for improved zinc-air battery efficiency. *J. Energy Storage* **2024**, *98*, 113008. [CrossRef]
99. Pradhan, A.K.; Halder, S.; Chakraborty, C. Pt-nanoparticles on ZnO/carbon quantum dots: A trifunctional nanocomposite with superior electrocatalytic activity boosting direct methanol fuel cells and zinc-air batteries. *J. Mater. Chem. A* **2025**, *13*, 243–256. [CrossRef]
100. Zhong, X.; Ye, S.; Tang, J.; Zhu, Y.; Wu, D.; Gu, M.; Pan, H.; Xu, B. Engineering Pt and Fe dual-metal single atoms anchored on nitrogen-doped carbon with high activity and durability towards oxygen reduction reaction for zinc-air battery. *Appl. Catal. B Environ.* **2021**, *286*, 119891. [CrossRef]
101. Yang, L.; Ma, J.; Liu, Y.; Ma, C.; Yu, X.; Chen, Z. Low platinum loading electrocatalyst supported on a carrier derived from carbon dots doped ZIF-67 for the ORR and zinc-air batteries. *Nanoscale* **2024**, *16*, 5433–5440. [CrossRef] [PubMed]
102. Luo, L.; Tang, R.; Su, L.; Kou, J.; Guo, X.; Li, Y.; Cao, X.; Cui, J.; Gong, S. Data-driven designed low Pt loading PtFeCoNiMnGa nano high entropy alloy with high catalytic activity for Zn-air batteries. *Energy Storage Mater.* **2024**, *72*, 103773. [CrossRef]
103. Wang, Y.; Luo, W.; Gong, S.; Luo, L.; Li, Y.; Zhao, Y.; Li, Z. Synthesis of High-Entropy-Alloy Nanoparticles by a Step-Alloying Strategy as a Superior Multifunctional Electrocatalyst. *Adv. Mater.* **2023**, *35*, 2302499. [CrossRef]
104. Jeevahan, J.; Chandrasekaran, M.; Joseph, G.B.; Durairaj, R.B.; Mageshwaran, G. Superhydrophobic surfaces: A review on fundamentals, applications, and challenges. *J. Coat. Technol. Res.* **2018**, *15*, 231–250. [CrossRef]
105. Xu, C.-X.; Zhang, J.-J.; Dou, H.-R.; Li, Y.-Z.; Li, D.-M.; Zhang, Y.-J.; Liu, B.; Inbaraj, P.; Huo, P.-P. Fe<sub>4</sub>N particles embedded in nitrogen-doped electrospun carbon nanofibers as efficient ORR catalysts for zinc-air battery. *Rare Met.* **2025**, *44*, 3156–3169. [CrossRef]
106. Xu, C.; Guo, C.; Liu, J.; Hu, B.; Chen, H.; Li, G.; Xu, X.; Shu, C.; Li, H.; Chen, C. Bioinspired Hydrophobicity Coupled with Single Fe-N<sub>4</sub> Sites Promotes Oxygen Diffusion for Efficient Zinc-Air Batteries. *Small* **2023**, *19*, 2207675. [CrossRef]
107. Cui, H.; Jiao, M.; Chen, Y.-N.; Guo, Y.; Yang, L.; Xie, Z.; Zhou, Z.; Guo, S. Molten-Salt-Assisted Synthesis of 3D Holey N-Doped Graphene as Bifunctional Electrocatalysts for Rechargeable Zn–Air Batteries. *Small Methods* **2018**, *2*, 1800144. [CrossRef]
108. Xi, Z.; Han, J.; Jin, Z.; Hu, K.; Qiu, H.-J.; Ito, Y. All-Solid-State Mg–Air Battery Enhanced with Free-Standing N-Doped 3D Nanoporous Graphene. *Small* **2024**, *20*, 2308045. [CrossRef] [PubMed]
109. Fu, K.; Ma, B.; Liu, J.; Zhou, M.; Xing, Y.; Wei, X.; Meng, F.; Liu, J. In situ green architecture of the 3D FeZn–N–C based electrocatalyst for efficient oxygen reduction. *Chem. Commun.* **2024**, *60*, 10366–10369. [CrossRef]

110. Sun, J.; Shen, M.; Chang, A.J.; Liang, C.; Xiong, C.; Hou, C.; Li, J.; Wang, P.; Li, J.; Huang, J. Cascade protection strategy for anchoring atomic FeN<sub>3</sub> sites within defect-rich wood carbon aerogel for high-performance Zn-air batteries and versatile application. *Chem. Eng. J.* **2025**, *503*, 158551. [[CrossRef](#)]
111. Zhao, P.; Zhang, L.; Chen, J.; Qiu, C.; Wang, B.; Li, J.; Zhang, K.; Yang, G. From wood to flexible Zn-air Battery: Fe<sub>3</sub>O<sub>4</sub> nanoparticles synergistic single iron atoms on N-doped carbon nanosheets electrocatalyst and Lignosulfonate-Functionalized gel electrolyte. *Chem. Eng. J.* **2024**, *484*, 149415. [[CrossRef](#)]
112. Wan, W.; Wang, Q.; Zhang, L.; Liang, H.-W.; Chen, P.; Yu, S.-H. N-, P- and Fe-tridoped nanoporous carbon derived from plant biomass: An excellent oxygen reduction electrocatalyst for zinc–air batteries. *J. Mater. Chem. A* **2016**, *4*, 8602–8609. [[CrossRef](#)]
113. Feng, Y.; Song, K.; Zhang, W.; Zhou, X.; Yoo, S.J.; Kim, J.-G.; Qiao, S.; Qi, Y.; Zou, X.; Chen, Z.; et al. Efficient ORR catalysts for zinc-air battery: Biomass-derived ultra-stable Co nanoparticles wrapped with graphitic layers via optimizing electron transfer. *J. Energy Chem.* **2022**, *70*, 211–218. [[CrossRef](#)]
114. Hao, M.; Dun, R.; Su, Y.; He, L.; Ning, F.; Zhou, X.; Li, W. In situ self-doped biomass-derived porous carbon as an excellent oxygen reduction electrocatalyst for fuel cells and metal–air batteries. *J. Mater. Chem. A* **2021**, *9*, 14331–14343. [[CrossRef](#)]
115. Jiang, M.; Fu, C.; Cheng, R.; Liu, T.; Guo, M.; Meng, P.; Zhang, J.; Sun, B. Interface engineering of Co<sub>3</sub>Fe<sub>7</sub>–Fe<sub>3</sub>C heterostructure as an efficient oxygen reduction reaction electrocatalyst for aluminum-air batteries. *Chem. Eng. J.* **2021**, *404*, 127124. [[CrossRef](#)]
116. Ma, L.; Hu, X.; Min, Y.; Zhang, X.; Liu, W.; Lam, P.K.S.; Li, M.M.J.; Zeng, R.J.; Ye, R. Microalgae-derived single-atom oxygen reduction catalysts for zinc-air batteries. *Carbon* **2023**, *203*, 827–834. [[CrossRef](#)]
117. Ma, L.-L.; Liu, W.-J.; Hu, X.; Lam, P.K.S.; Zeng, J.R.; Yu, H.-Q. Ionothermal carbonization of biomass to construct sp<sup>2</sup>/sp<sup>3</sup> carbon interface in N-doped biochar as efficient oxygen reduction electrocatalysts. *Chem. Eng. J.* **2020**, *400*, 125969. [[CrossRef](#)]
118. Jiao, C.; Xu, Z.; Shao, J.; Xia, Y.; Tseng, J.; Ren, G.; Zhang, N.; Liu, P.; Liu, C.; Li, G.; et al. High-Density Atomic Fe–N<sub>4</sub>/C in Tubular, Biomass-Derived, Nitrogen-Rich Porous Carbon as Air-Electrodes for Flexible Zn–Air Batteries. *Adv. Funct. Mater.* **2023**, *33*, 2213897. [[CrossRef](#)]
119. Niu, J.; Liu, Y.; Wang, X.; Liu, J.; Zhao, Z.; Liu, X.; Ostrikov, K. Biomass-Derived Bifunctional Cathode Electrocatalyst and Multiadaptive Gel Electrolyte for High-Performance Flexible Zn–Air Batteries in Wide Temperature Range. *Small* **2023**, *19*, 2302727. [[CrossRef](#)]
120. Chen, Z.; Zou, Y.; Chen, H.; Zhang, K.; Hui, B. Bamboo-Modulated Helical Carbon Nanotubes for Rechargeable Zn-Air Battery. *Small* **2024**, *20*, 2307776. [[CrossRef](#)]
121. Zhou, M.; Fu, K.; Xing, Y.; Liu, J.; Meng, F.; Wei, X.; Liu, J. 500 mW cm<sup>-2</sup> underwater Zn-H<sub>2</sub>O<sub>2</sub> batteries with ultrafine edge-enriched electrocatalysts. *Sci. China Mater.* **2024**, *67*, 2908–2914. [[CrossRef](#)]
122. Chen, P.; Zhang, K.; Tang, D.; Liu, W.; Meng, F.; Huang, Q.; Liu, J. Recent Progress in Electrolytes for Zn–Air Batteries. *Front. Chem.* **2020**, *8*, 372. [[CrossRef](#)] [[PubMed](#)]
123. Siahrostami, S. H<sub>2</sub>O<sub>2</sub> electrosynthesis and emerging applications, challenges, and opportunities: A computational perspective. *Chem Catal.* **2023**, *3*, 100568. [[CrossRef](#)]
124. Liu, J.; Zhou, M.; Jin, K.; Li, J.; Meng, F.; Wei, X. Beyond metal–air battery, emerging aqueous metal–hydrogen peroxide batteries with improved performance. *Battery Energy* **2024**, *3*, 20230049. [[CrossRef](#)]
125. Brodrecht, D.J.; Rusek, J.J. Aluminum–hydrogen peroxide fuel-cell studies. *Appl. Energy* **2003**, *74*, 113–124. [[CrossRef](#)]
126. Hasvold, O.; Johansen, K.H. The alkaline aluminium hydrogen peroxide semi-fuel cell for the HUGIN 3000 autonomous underwater vehicle. In Proceedings of the 2002 Workshop on Autonomous Underwater Vehicles, San Antonio, TX, USA, 21 June 2002; pp. 89–94.
127. Xu, L.; Liu, J.; Chen, P.; Wang, Z.; Tang, D.; Liu, X.; Meng, F.; Wei, X. High-Power Aqueous Zn-H<sub>2</sub>O<sub>2</sub> Batteries for Multiple Applications. *Cell Rep. Phys. Sci.* **2020**, *1*, 100027. [[CrossRef](#)]
128. Sun, L.; Wen, F.; Shi, L.; Li, S. Pd and CoO<sub>x</sub> decorated reduced graphene oxide self-assembled on Ni foam as Al–H<sub>2</sub>O<sub>2</sub> semi-fuel cells cathodes. *J. Alloys Compd.* **2020**, *815*, 152361. [[CrossRef](#)]
129. Shu, C.; Wang, E.; Jiang, L.; Tang, Q.; Sun, G. Studies on palladium coated titanium foams cathode for Mg–H<sub>2</sub>O<sub>2</sub> fuel cells. *J. Power Sources* **2012**, *208*, 159–164. [[CrossRef](#)]
130. Liu, X.; Wang, J.; Lv, P.; Zhang, Y.; Li, J.; Wei, Q. Gel polymer electrolyte based on deep eutectic solvent in flexible Zn-air batteries enables dendrite-free Zn anode. *Energy Storage Mater.* **2024**, *69*, 103382. [[CrossRef](#)]
131. Li, C.-P.; Zhang, W.-Y.; Gao, L.-X.; Zhang, D.-Q. A patching reinforcement strategy for hybrid surfactants as electrolyte additives with excellent performance in aluminum-air batteries. *J. Power Sources* **2023**, *584*, 233604. [[CrossRef](#)]
132. Zhang, D.; Hu, W. Improving Cycle Life of Zinc–Air Batteries with Calcium Ion Additive in Electrolyte or Separator. *Nanomaterials* **2023**, *13*, 1864. [[CrossRef](#)]
133. Wan, H.; Bai, Q.; Peng, Z.; Mao, Y.; Liu, Z.; He, H.; Wang, D.; Xie, J.; Wu, G. A high power Li-air battery enabled by a fluorocarbon additive. *J. Mater. Chem. A* **2017**, *5*, 24617–24620. [[CrossRef](#)]
134. Jianming, R.; Tao, L.; Jiao, Z.; Min, J.; Qing, D.; Chaopeng, F. Spray-formed commercial aluminum alloy anodes with suppressed self-corrosion for Al-Air batteries. *J. Power Sources* **2022**, *524*, 231082. [[CrossRef](#)]

135. Meng, A.; Sun, Y.; Cheng, W.; Huang, L.; Chen, Y. Discharge performance of Al-0.1Sn-0.1In-0.05Ga alloy for Al-air battery anodes. *J. Energy Storage* **2024**, *81*, 110414. [[CrossRef](#)]
136. Liu, J.; Xing, Y.; Ma, B.; Wei, X.; Li, S.; Li, D.; Meng, F.; Deng, W.; Liu, J. Tripod-Linked Molecular Armor for Low-Overpotential Al-Air Batteries. *ACS Electrochem.* **2025**, *1*, 826–831. [[CrossRef](#)]
137. Li, X.; Li, J.; Zhang, D.; Gao, L.; Qu, J.; Lin, T. Synergistic effect of 8-aminoquinoline and ZnO as hybrid additives in alkaline electrolyte for Al-air battery. *J. Mol. Liq.* **2021**, *322*, 114946. [[CrossRef](#)]
138. Wei, M.; Wang, K.; Pei, P.; Zuo, Y.; Zhong, L.; Shang, N.; Wang, H.; Chen, J.; Zhang, P.; Chen, Z. An enhanced-performance Al-air battery optimizing the alkaline electrolyte with a strong Lewis acid ZnCl<sub>2</sub>. *Appl. Energy* **2022**, *324*, 119690. [[CrossRef](#)]
139. Jiang, H.; Yu, S.; Li, W.; Yang, Y.; Yang, L.; Zhang, Z. Inhibition effect and mechanism of inorganic-organic hybrid additives on three-dimension porous aluminum foam in alkaline Al-air battery. *J. Power Sources* **2020**, *448*, 227460. [[CrossRef](#)]
140. Deyab, M.A. Effect of nonionic surfactant as an electrolyte additive on the performance of aluminum-air battery. *J. Power Sources* **2019**, *412*, 520–526. [[CrossRef](#)]
141. Huang, Y.; Shi, W.; Guo, L.; Zhang, Q.; Wang, K.; Zheng, X.; Verma, C.; Qiang, Y. Corrosion inhibition of L-tryptophan on Al-5052 anode for Al-air battery with alkaline electrolyte. *J. Power Sources* **2023**, *564*, 232866. [[CrossRef](#)]
142. Zhang, W.; Cai, S.; Zhang, D.; Gao, L. Excellent performance of 8-hydroxyquinoline and alkyl polyglycolides hybrid electrolyte additives on aluminum-air battery. *Chem. Eng. J.* **2023**, *472*, 145139. [[CrossRef](#)]
143. Zhu, C.; Yang, H.; Wu, A.; Zhang, D.; Gao, L.; Lin, T. Modified alkaline electrolyte with 8-hydroxyquinoline and ZnO complex additives to improve Al-air battery. *J. Power Sources* **2019**, *432*, 55–64. [[CrossRef](#)]
144. Kang, Q.X.; Zhang, T.Y.; Wang, X.; Wang, Y.; Zhang, X.Y. Effect of cerium acetate and L-glutamic acid as hybrid electrolyte additives on the performance of Al-air battery. *J. Power Sources* **2019**, *443*, 227251. [[CrossRef](#)]
145. Guo, L.; Zhu, L.; Huang, Y.; Tan, Y.; Ritacca, A.G.; Zheng, X.; Leng, S.; Wang, B. Self-assembly of an amino acid derivative as an anode interface layer for advanced alkaline Al-air batteries. *Phys. Chem. Chem. Phys.* **2024**, *26*, 10892–10903. [[CrossRef](#)]
146. Guo, L.; Zhang, Q.; Huang, Y.; Sun, R.; Zhang, R.; Saji, V.S.; Chang, J.; Zheng, X.; Makin Adam, A.M. Regulating the Helmholtz plane by trace ionic liquid additive for advanced Al-air battery. *J. Power Sources* **2025**, *625*, 235672. [[CrossRef](#)]
147. Kang, Q.X.; Wang, Y.; Zhang, X.Y. Experimental and theoretical investigation on calcium oxide and L-aspartic acid as an effective hybrid inhibitor for aluminum-air batteries. *J. Alloys Compd.* **2019**, *774*, 1069–1080. [[CrossRef](#)]
148. Qiu, D.; Li, B.; Zhao, C.; Dang, J.; Chen, G.; Qiu, H.; Miao, H. A review on zinc electrodes in alkaline electrolyte: Current challenges and optimization strategies. *Energy Storage Mater.* **2023**, *61*, 102903. [[CrossRef](#)]
149. Wang, J.; Panchal, A.A.; Canepa, P. Strategies for fitting accurate machine-learned inter-atomic potentials for solid electrolytes. *Mater. Futures* **2023**, *2*, 015101. [[CrossRef](#)]
150. Wang, T.; Yang, T.; Luo, D.; Fowler, M.; Yu, A.; Chen, Z. High-Energy-Density Solid-State Metal–Air Batteries: Progress, Challenges, and Perspectives. *Small* **2024**, *20*, 2309306. [[CrossRef](#)]
151. Sun, P.; Chen, J.; Huang, Y.; Tian, J.-H.; Li, S.; Wang, G.; Zhang, Q.; Tian, Z.; Zhang, L. High-Strength agarose gel electrolyte enables long-endurance wearable Al-air batteries with greatly suppressed self-corrosion. *Energy Storage Mater.* **2021**, *34*, 427–435. [[CrossRef](#)]
152. Cui, W.; Ma, C.; Lei, X.; Lv, Y.; Zhang, Q.; Guan, W.; Liu, X. Gel electrolyte with dimethyl sulfoxide confined in a polymer matrix for Li-air batteries operable at sub-zero temperature. *J. Power Sources* **2023**, *577*, 233264. [[CrossRef](#)]
153. Emley, B.; Wu, C.; Zhao, L.; Ai, Q.; Liang, Y.; Chen, Z.; Guo, L.; Terlier, T.; Lou, J.; Fan, Z.; et al. Impact of fabrication methods on binder distribution and charge transport in composite cathodes of all-solid-state batteries. *Mater. Futures* **2023**, *2*, 045102. [[CrossRef](#)]
154. Shang, Z.; Zhang, H.; Liang, J.; You, Z.; Wang, R.; Wan, L.; Lei, D.; Li, Z. Highly adhesive hydrogel electrolytes driven by adenosine monophosphate and Fe<sup>3+</sup> for high-voltage asymmetric flexible zinc-air batteries. *Energy Storage Mater.* **2024**, *71*, 103599. [[CrossRef](#)]
155. Chen, Y.; He, S.; Rong, Q. Stretchable, anti-drying, and self-healing hydrogel electrolytes for thermal adaptive zinc-air batteries with robust electrolyte/electrode interfaces. *Mater. Today Chem.* **2023**, *33*, 101726. [[CrossRef](#)]
156. Zhang, Y.; Wu, D.; Huang, F.; Cai, Y.; Li, Y.; Ke, H.; Lv, P.; Wei, Q. “Water-in-Salt” Nonalkaline Gel Polymer Electrolytes Enable Flexible Zinc-Air Batteries with Ultra-Long Operating Time. *Adv. Funct. Mater.* **2022**, *32*, 2203204. [[CrossRef](#)]

**Disclaimer/Publisher’s Note:** The statements, opinions and data contained in all publications are solely those of the individual author(s) and contributor(s) and not of MDPI and/or the editor(s). MDPI and/or the editor(s) disclaim responsibility for any injury to people or property resulting from any ideas, methods, instructions or products referred to in the content.